SEISMIC MODELING OF THE EAGLE FORD — HOW DO CHANGES OF GEOLOGICAL FACIES AFFECT THE SEISMIC RESPONSE?

A Thesis

by

APRIL MARIE RIDER

Submitted to the Office of Graduate and Professional Studies of
Texas A&M University
in partial fulfillment of the requirements for the degree of

MASTER OF SCIENCE

Chair of Committee,	Richard Gibson
Committee Members,	Juan Carlos Laya Pereira
	Michael King
Head of Department,	Michael Pope

August 2018

Major Subject: Geophysics

ABSTRACT

This paper utilizes synthetic models of the Eagle Ford to identify how variation of lithological facies across the regional extent of the Eagle Ford affects its seismic response. I apply three different modeling methods at seven different locations across the Eagle Ford: 1) Linear regression of petrophysical cross-plots that extrapolate velocity and density log values through calculated brightness logs treated as gamma ray proxies, 2) synthetic seismograms convolved with 30Hz and 60Hz Ricker wavelets, and 3) simplified upscaled models derived by an automated log blocking code based on a Monte Carlo procedure. Results reveal acceptable synthetic seismograms representative of the geology can be created using unconventional methods. The regional seismic responses exhibit similar time duration and seismic characters, but the number of cycles within the Eagle Ford varies with respect to internal variation and the interpreted boundaries change with respect to the facies distribution.

ACKNOWLEDGMENTS

I would like to thank Richard Gibson for being my adviser, along with Mike King and Juan Carlos Laya for agreeing to serve on my committee. I would also like to thank Art Donovan, Drew Davis, and Sireesh Dadi, without their data, I could not have completed my thesis. Special thanks to UnYoung Lim, your help throughout this process was invaluable. Lastly thank you to my parents and friends who never stopped supporting and believing in me.

CONTRIBUTORS AND FUNDING SOURCES

Contributors

This work was supported by a thesis committee consisting of Professor Richard Gibson and Professor Juan Carlos Laya of the Department of Geology & Geophysics and Professor Mike King of the Department of Petroleum Engineering.

Well logs were provided by Texas A&M University and Professor Art Donovan. Photogrammetry data used to conduct a portion of the research was provided by the research from Drew Davis, and the upscaling code applied in this thesis was developed by Sireesh Dadi.

All other work conducted for the thesis was completed by the student independently.

Funding Sources

Graduate study was supported by a scholarship from the Coastal Bend Geophysics Society and through a Teacher's Assistant for geology labs.

NOMENCLATURE

EF	Eagle Ford
AC	Austin Chalk
SR	Scott Ranch
CN	Colonel Neck
CB	Colonel Bend
GR	Gamma Ray
DTCO	Delta Time Compressional (Slowness)
RHOZ	Bulk Density
ILD	Deep Induction Log (Resistivity)
CALI	Caliper
NPHI	Neutron Porosity
SP	Spontaneous Potential
UAV	Unmanned Aerial Vehicles
DOM	Digital Outcrop Models
RGB	Red, Green, Blue
VSP	Vertical Seismic Profile
Vp	P-Velocity (Compressional)
Vs	S-Velocity (Shear)
RJMCMC	Reverse Jump Markov Chain Monte Carlo
PPD	Posterior Probability Distribution
RMS	Root Mean Square

TABLE OF CONTENTS

Page

LIST OF FIGURES

FIGURE Page

LIST OF TABLES

TABLE Page

1. INTRODUCTION

With unconventional reservoirs continuing to provide new opportunities for petroleum companies across the globe, it is important to understand how these unique reservoirs operate. Shale plays are complex geologic systems with respect to anisotropy, micro-scale fabric, and thin bed issues, and often require long horizontal drilling paths to exploit "sweet spots" (Donovan et al., 2016 [7] and Ren, 2016 [8]). The Eagle Ford has been a prolific unconventional reservoir since 2008, is one of the most active areas in the world, and is the formation of interest for this study. There is a wide range of geologic information available across its entire depositional extent from analysis of the distribution of variation of lithological facies (Davis, 2017 [3]; Dawson, 2000 [9]; Basu et al., 2012 [10]; Donovan et al., 2012 [6]; Breyer et al., 2013 [11]; Workman and Grammer, 2013 [12]; Tinnin et al., 2014 [13]; and Breyer, 2015 [14]), variations in production on a regional scale related to structure and rock properties (Hammes et al, 2016 [1]; Hentz and Ruppel, 2010 [15]; Matsutsuyu, 2011 [16]; and Breyer et al., 2013 [11]; Ogiesoba & Hammes, 2014 [17]), and geophysical investigations into the thin bed resolution, anisotropy, and attribute analysis for identifying sweet spots (Treadgold et al, 2011 [18]; Ogiesoba & Hammes, 2014 [17]; Ren, 2016 [8]; Santogrossi, 2015 [19]; Chen et al., 2016 [20]).

My thesis provides the first public geophysical study on Eagle Ford outcrops, which are considered reservoir analogs, and connects the fine-scaled geological details with the less detailed seismic responses over the Eagle Ford's regional extent without the spatial limitation encountered with seismic surveys. I apply three Eagle Ford models on two different scales. The first model uses linear regression to convert photogrammetry data collected at outcrops to seismic inputs (velocity and density logs) at two localized outcrops in Lozier Canyon where well information and seismic data are not readily available. The other two types of models are 1D synthetic seismograms and upscaled "best-fit" impedance models generated from an automated log blocking code developed by Sireesh Dadi (2016) [21], and are applied regionally at seven different Eagle Ford locations spanning across 250 kilometers.

Together, my results provide a unique approach to geophysically modeling the responses of sections studies in outcrops without the need of drilling wells or acquiring seismic surveys, reveal patterns linking the Eagle Ford lithology to its seismic response, allows for the comparison of the subsurface Eagle Ford seismic responses with their outcrop analogs, and addresses topics such as:

1. The relationship between brightness, gamma ray, velocity, and density.
2. The regional variation of the Eagle Ford seismic response.
3. Are the changes in the Eagle Ford's seismic response related to the distribution of lithologic facies?

2. BACKGROUND

The Eagle Ford was deposited in the Late Cretaceous at a maximum flooding surface of a transgressive sequence during the Late Cenomanian through the Turonian and represents one complete depositional sequence (Hammes et al, 2016 [1]; Davis, 2017 [3]; Gardner et al, 2013 [22]). The Eagle Ford covers more than 11000 square miles in South Texas and composition ranges from marls to limestones (Ogiesoba & Hammes, 2014 [17]; Treadgold et al., 2011 [18]). Overall thicknesses can range anywhere from 40 to 400 feet and correlates with the on-lap and truncation of the overlying and underlying unconformities (Ogiesoba & Hammes, 2014 [17]; Donovan & Staerker, 2010 [2]). The Eagle Ford crops out to the north, dips southward, and can reach up to depths of 16000 feet (4900 meters) towards the east and south.

2.1 Stratigraphy & Terminology

With models focusing on the Eagle Ford, only the formations directly overlying and underlying the Eagle Ford are relevant for this study. The Eagle Ford unconformably lies between the Buda Limestone below, and the Austin Chalk above (Figure 2.1), all of which are Cretaceous in age.

Many interpretations have been made to describe the internal structure of the Eagle Ford and sub-divide it into different units (Hazzard, 1959 [23]; Freeman, 1961 [24]; Freeman, 1968 [25]; Trevino, 1988 [26]; Pessagno, 1969 [27]; Lock & Peschier, 2006 [28]; and Donovan & Staerker, 2010 [2]). To be consistent with the work already done at the outcrop at Lozier Canyon, I used the nomenclature described in Donovan & Staerker (2010) [2]. Donovan subdivided the Eagle Ford into 5 main sub-facies labeled A through E using Eagle Ford outcrops in Lozier Canyon. Facies A is chronologically the oldest and E is the youngest. Facies A and B were deposited in an anoxic environment and facies C-E in an oxic environment. The contact between Facies C and B separates the Upper Eagle Ford from the Lower Eagle Ford. Facies B has been the main target for petroleum companies, because it has the highest total organic content within the Eagle Ford and because facies A is not present in the subsurface (Davis, 2017 [3]; Donovan et al, 2015 [29];

Wehner et al, 2015 [30]). Each of the facies, when present, were treated as individual layers in the seismic models. Table 2.1 summarizes the "layers" used in the models along with their lithologies, environment of depositions, and typical log behaviors.

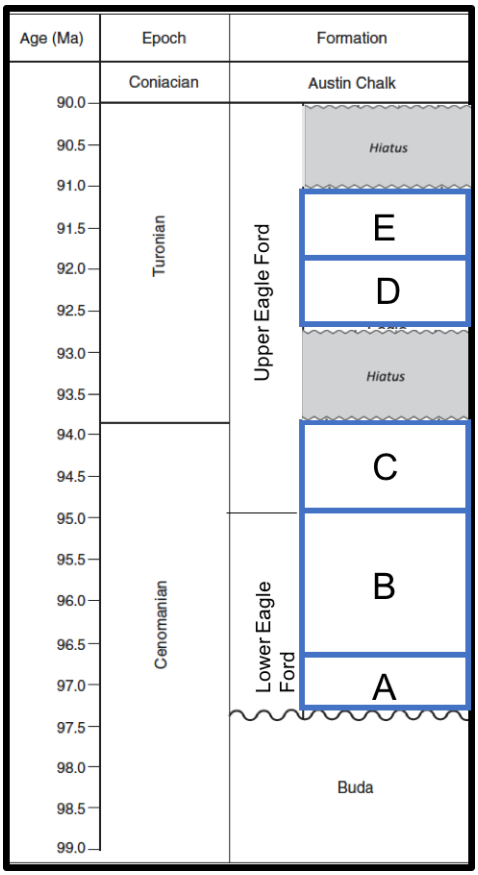

Figure 2.1: Stratigraphic column of Cretaceous aged formations included in Eagle Ford models. Modified from Hammes et al (2016) [1] to include nomenclature from Donovan & Staerker (2010) [2] dividing the Eagle Ford into 5 different sub-facies labeled A-E.

2.2 Key Structures & Depositional Areas

During the Cretaceous, temperatures and sea levels were at a high giving way to carbonate factories around the world (Hammes et al, 2016 [1]; Davis, 2017 [3]; Barron & Washington, 1984 [31]). The regional extent of the Eagle Ford relevant to this paper was deposited on the coalesced Comanche Platform formed when a transgressive sequence connected the Tethys Seaway (modern

EF Facies Information			
Facies:	**Lithology:**	**Environment:**	**Etc:**
Austin Chalk	Bioturbated wackestone, interbedded chalks and marls	Shallow open marine shelf	Contact with EF tends to be gradational on logs
E	Yellow ochre, thin bedded limestones (grainstones) interbedded with calcareous mudstones	Oxic/ open shelf/ above storm wave base	Thin in subsurface well logs âĂŞ share similar characteristics with Austin Chalk and Facies D
D	Pale-yellow ochre, echinoid bearing marls and nodular limestones	Oxic/ open shelf/ above storm wave base	Thin in subsurface well logs âĂŞ share similar characteristics with Austin Chalk and Facies D
C	Medium gray thick bedded limestones (packstones/ grainstones) interbedded with mudstones	Oxic/ open shelf/ above storm wave base	Considered secondary reservoir unit in some areas
B	Black organic-rich calcareous mudstones with scattered limestone (grainstone)	Anoxic/ restricted shelf/ episodically above storm wave base	Typically highest total organic content (TOC) values/ Main reservoir unit/ increased gamma ray values
A	Light gray cross-stratified limestones (grainstones/packstones) separated by thin calcareous mudstone beds	Anoxic/ restricted shelf/ episodically above storm wave base	Mostly absent in subsurface
Buda Limestone	Bioturbated wackestone	Shallow sub-tidal storm deposits	Sharp boundary on logs marked by decrease in gmma ray/resistivity and increase in velocity/density

Table 2.1: Table summarizing the geologic background of each formation or facies that will be incorporated into the model (Donovan et al, 2012; Davis, 2016).

Gulf of Mexico) to the Arctic Ocean (Davis, 2017 [3]; Hill, 1987 [32]; Scholle et al, 1983 [33]; Workman, 2013 [4]; Gardner et al, 2013 [22]; Hart, 2015 [34]). The Eagle Ford is bounded by the Maverick Basin to the west, the San Marcos Arch to the east, and the Sligo Reef Margin to the south illustrated in Figure 2.2. The Maverick Basin is a topographic low and contains thicker Eagle Ford sections resultant from the increased accommodation space. The San Marcos Arch marks the boundary between the Eagle Ford from the more clay-prone Eaglebine, and the Sligo Reef Margin represents the furthest southern extent of the Eagle Ford, after which it thins out (Hammes et al, 2016 [1]; Donovan et al, 2013 [35]; Goldhammer & Johnson, 1999 [36]; Hentz & Ruppel, 2010 [15]; Ewing, 2001 [37]). There is a separation of tectonic regimes represented by the Frio River Line shown in Figure 2.2 where west of the line is dominated by compressional faults from the Laramide Orogeny and east of the line is dominated by a northeast striking extensional regime (Hammes et al, 2016 [1]; Ewing, 2010 [37]; Goldhammer & Johnson, 2001 [38]).

2.3 Study Area & Available Data

Subsurface wells and outcrop data of the Eagle Ford were integrated into this study from 7 locations: 4 subsurface well sites distributed across four different counties (Dimmit, La Salle, Live Oak, and Karnes) and 3 outcrop sites located in Lozier Canyon (Terrell County) (Figure 2.3). Lozier Canyon is a dry tributary that once fed into the Rio Grande River in Terrell County along the US-Mexican border. Though many outcrops were exposed, this thesis only focuses on the Scott Ranch, Colonel Neck, and Colonel Bend locations (Figure 2.4). BP drilled a research well directly behind the Scott Ranch outcrop face which provided key constraints for developing the geophysical models used to compute velocity and density logs at the Colonel Neck and Colonel Bend locations where there is a lack of conventional well data. Colonel Neck and Colonel Bend are approximately 6 miles south of Scott Ranch where an oxbow lake almost formed. Davis (2017) [3] mapped the lateral changes of the facies defined by Donovan & Staerker (2010) [2] across Lozier Canyon using photogrammetry data and is the first scientist to publish research on Colonel Neck and Colonel Bend. All three outcrop sites also have calculated brightness logs using the photogrammetry data.

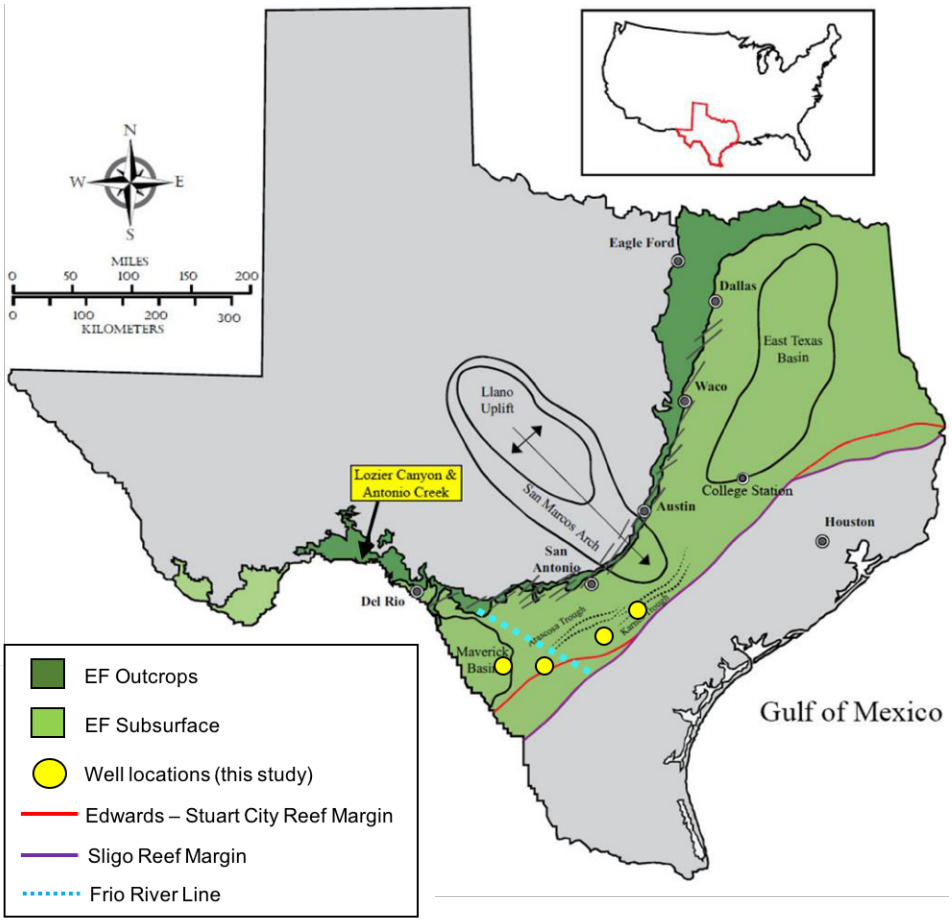

Figure 2.2: Distribution of the Eagle Ford relative to the main structures. The Frio River Line represents the boundary between two different tectonic regimes (Modified from Davis, 2017 [3]; Workman, 2013 [4]; and Geology of Texas Map, 1992 [5]). For reference, study locations are shown in yellow.

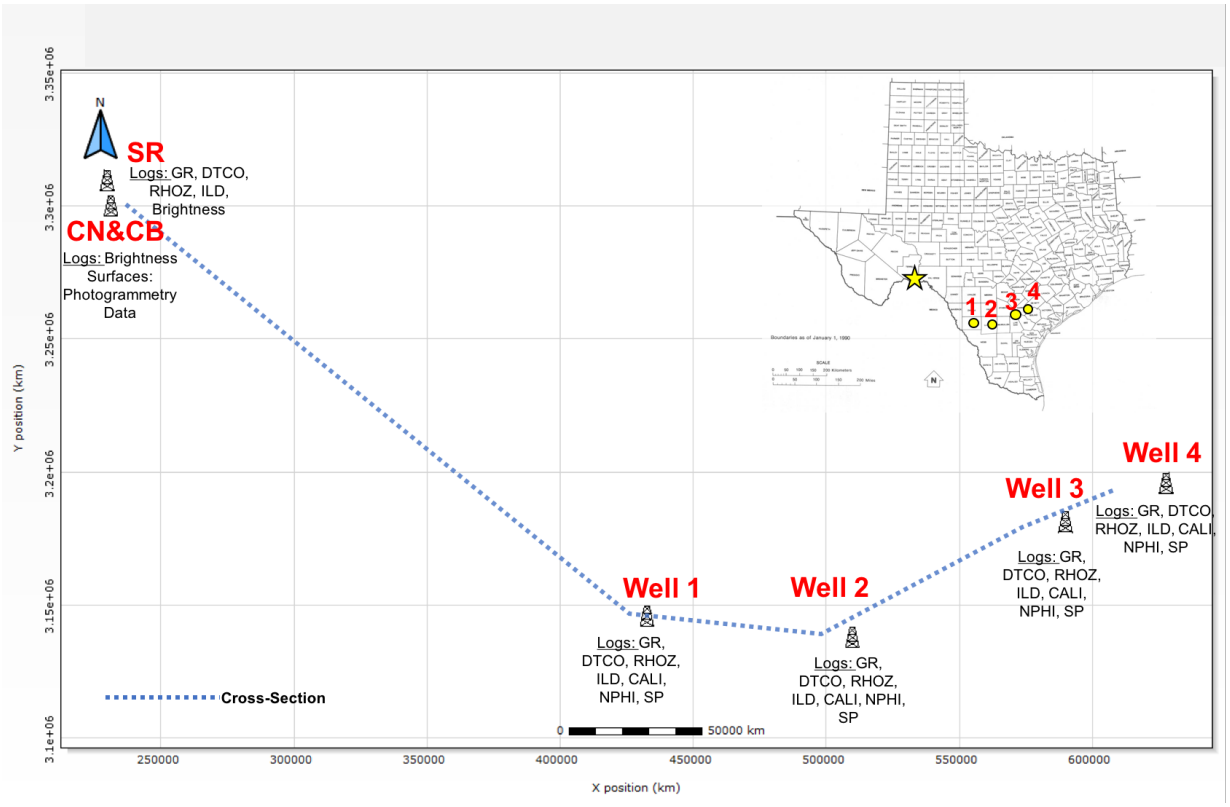

Figure 2.3: Map showing the seven different study area locations across southern Texas.

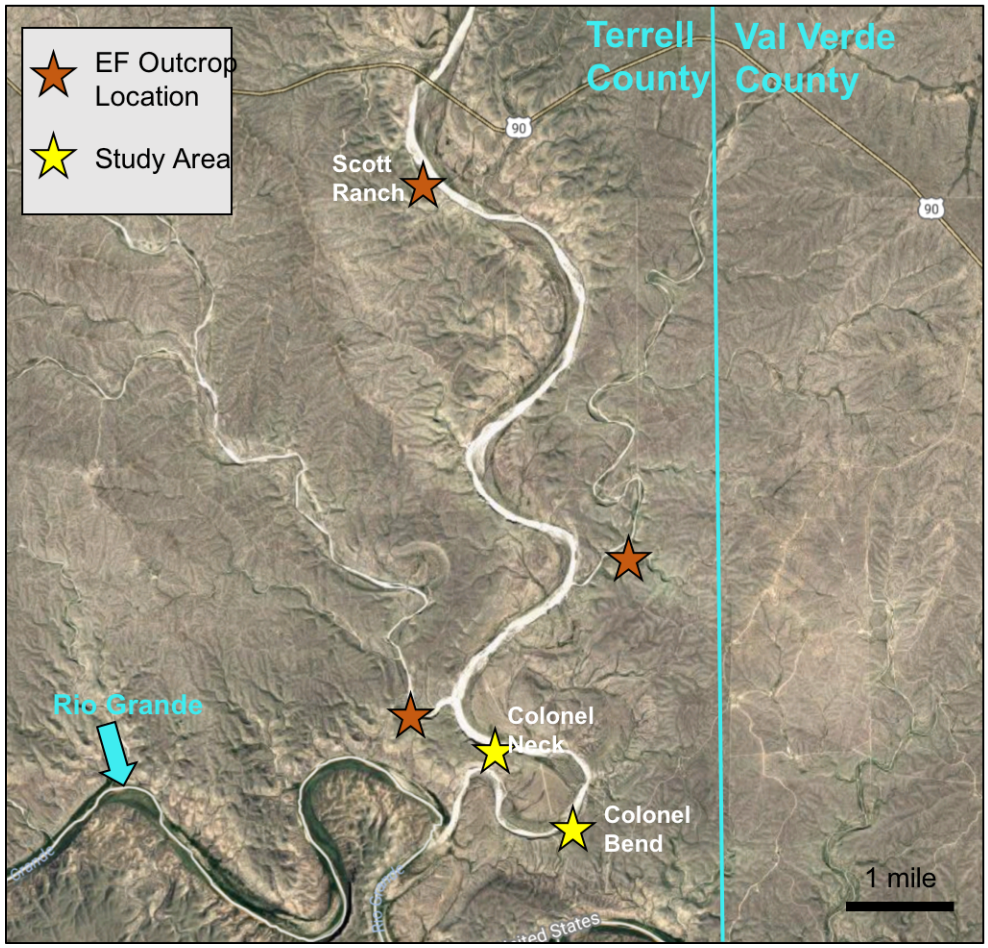

Figure 2.4: Aerial view of Lozier Canyon. The stars indicate exposed outcrops that have been previously studied and the yellow stars are the locations that will be incorporated into this study.

3. METHODS

Each research step builds off the previous step and increases in scale. I first interpret layer boundaries at the four available subsurface wells which provide the data points used to correlate Eagle Ford rock properties. I then create geophysical models to extrapolate seismic quantities on to outcrop faces. And finally, I calculate 1D synthetic seismograms and upscaled models at 7 locations across southern Texas, including the outcrops with extrapolated logs, to understand how the responses regionally vary across south Texas with respect to the changing lithologies and facies distribution.

3.1 Generating Outcrop Logs

3.1.1 Interpreting Well Data

Each location in the dataset samples a different section of the Eagle Ford each with varying spatial locations, overall thickness, and distribution of the individual facies A-E. The Scott Ranch well, previously interpreted by Donovan et al (2012) [6], along with other regional logs interpreted by Hammes et al (2016) [1], were used as references for identifying similar log patterns on Wells 1-4. The formation tops mapped on each well include (in order of increasing age/ decreasing depth):

- Bottom Austin Chalk/ Top Eagle Ford
- Top Facies D
- Top Facies C
- Top Facies B
- Top Buda Limestone

Facies A is not included in the interpretation for Wells 1-4 because of its absence in the subsurface. Figure 3.1 presents the cross section of the five wells with the interpreted Eagle Ford boundaries.

The Scott Ranch well depicts the interpretation from Donovan et al (2012) [6] and Wells 1-4 depict my interpretation. Table 3.1 lists the spatial information and interpreted thicknesses for facies A-E for each study location.

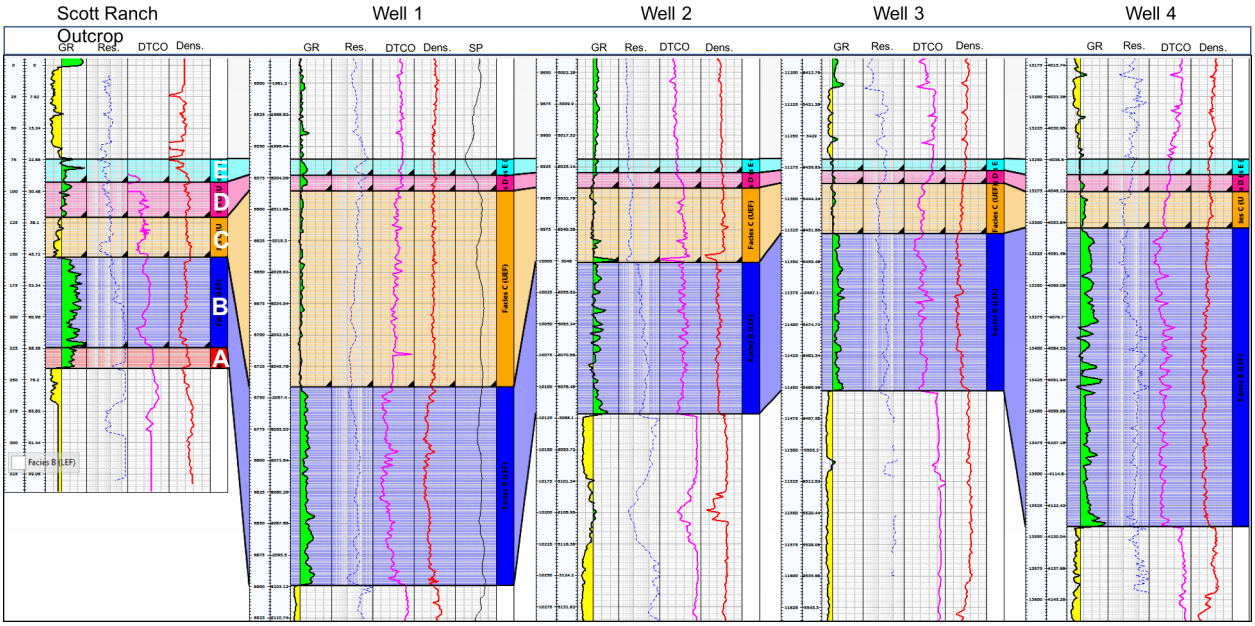

Figure 3.1: Cross section from line illustrated in Figure 2.3 from west to east for the 5 wells used in this study. The Eagle Ford boundaries mapped on the Scott Ranch well were taken from Donovan et al (2012) [6] and Wells 1-4 show my interpretation.

3.1.2 Brightness Logs

At the Colonel Neck and Colonel Bend outcrops where there is a lack of conventional well data, density and velocity values were extrapolated using brightness logs constructed from photogrammetry data. Photogrammetry is a technique that uses 2-D images with overlapping camera positions to project 3-D data (Birch, 2006 [39]; Bemis et al, 2014 [40]). Davis (2017) [3] used Unmanned Aerial Vehicles (UAVs) to collect thousands of high resolution photos of Lozier Canyon to construct Digital Outcrop Models (DOMs). Brightness logs at the Scott Ranch, Colonel Neck, and Colonel Bend outcrops were created by analyzing red, green, and blue color values (RGB) on

Eagle Ford Well Data								
Well Name:	**County:**	**Start Depth:**	**Approx. Thick.**	**Facies A**	**Facies B**	**Facies C**	**Facies D**	**Facies E**
Scott Ranch	Terrell	Surface	54	6	22.5	10.8	6	8.8
Colonel Neck	Terrell	Surface	61	6,8	24.8	13.2	9.5	6.5
Colonel Bend	Terrell	Surface	66	6.7	27.1	14.5	8.2	9.2
1	Dimmit	2000	103	N/A	48	47.6	3.4	3.8
2	La Salle	3023	62	N/A	36.5	17.9	3.8	3.4
3	Live Oak	3435	56	N/A	38.1	12.2	3	2.7
4	Karnes	4039	89	N/A	72.5	8.9	4	3.6

Table 3.1: Table summarizing the thicknesses of individual facies and overall thickness of the Eagle Ford for the 7 study locations. The Scott Ranch thicknesses were taken from Donovan et al (2012) [6] interpretation, Colonel Neck and Colonel Bend used interpretations from Davis (2017) [3], and wells 1-4 are based on my interpreted boundaries shown in Figure 5. (All values are in meters).

a composite section taken from the high-resolution photos that avoided irregular lighting, debris, and vegetation (Davis, 2017) [3].

$$Brightness = \frac{Red + Blue + Green}{3} \tag{3.1}$$

The Brightness values range from 0 to 255, where 0 is black and 255 is white. Russell (1945) [41] first determined that color could be related to radioactive material in material in shales and McNeal (1959) [42] showed that the purest limestones have the lightest colors. Combining these two studies, Davis (2017) [3] concluded that the Brightness logs could serve as a gamma ray proxy where the lower brightness values correspond with higher radioactive materials (shales) and the brighter values correspond with less radioactive material (limestones).

3.1.3 Correlating Rock Properties

Cross-plots were populated with Eagle Ford log values from the 5 well locations defined in Figure 3.1 to develop four models mathematically describing the relationship between brightness with

velocity and density. Discrepancies in the sampling rates between the typical logging techniques (0.152 meter) with the brightness logs calculated from photogrammetry data (0.008 meter) were accounted for by interpolating the brightness logs into a continuous line and re-discretizing the log every 0.152 meter, ensuring the same geological point is sampled on both the brightness and gamma ray logs. When available, other petrophysical properties such as resistivity, spontaneous potential, neutron porosity, caliper, etc., were incorporated into the cross-plots to definitively eliminate anomalous data points specific to individual well sites not representative of the overall Eagle Ford.

Correlation coefficients were calculated for each plot to determine the strength and type of relationship between the two variables, along with a combination of linear and non-linear regression models to predict values for the dependent variables (Y) based on the independent variables (X). For the regression models in this paper, the Y variable is only dependent on one independent variable. Using a least squares method, the regression fit either a straight line or exponential curve to the data that best predicted the dependent variable.

The coefficient of determination, R^2, is a statistical measure of the variability of Y that is explained by the variability of X through the relationship (Zou et al, 2003 [43]). The value varies between 0 and 1, where the closer the fraction is to 1, the more variability the model describes and is used to help determine which model to use.

3.2 Computation of Geophysical Models

3.2.1 Synthetic Seismograms

Synthetic seismograms were calculated using a forward model using a propagator matrix approach (Gibson & Hwang, 2009 [44]; Dadi, 2014 [45]) where the velocity and density logs were convolved with a 30Hz and 60Hz Ricker wavelet. These two frequencies were chosen because 30Hz is a frequency one would see in seismic surveys and 60Hz will provide more detail and is a frequency commonly seen in Vertical Seismic Profile (VSP) data. Synthetics allow for a direct comparison of the Eagle Ford response between locations free of noise encountered with acquisi-

tion and processing techniques and can provide constraints for the interpretation of seismic surveys (Christensen & Szymanski, 1991 [46]).

To keep the representation of the synthetic responses of the Eagle Ford consistent across all seven locations, I formatted the input logs to include the velocity (Vp and Vs) and density values for the Eagle Ford sandwiched in-between 300 feet (91 meters) of "padding" representative of average Austin Chalk and Buda Limestone values. Modeling the Austin Chalk and Buda Limestone using constant values eliminated their potential influence on the seismic response other than their interaction with the Eagle Ford boundaries. Inputs for the Eagle Ford Vp and density values at each location were dependent on the type of data available, and were taken either from the drilled well logs, or extrapolated log values. There was a the lack of Vs data at all locations, and so values were assigned using the relationship: $Vs = \frac{Vp}{2}$.

3.2.2 Upscaled Models

Log upscaling, or "log-blocking", is a means to compare high frequency elastic measurements to those measurements obtained from lower frequencies (Dadi et al., 2016 [21]). It takes a fine-scaled well log and develops a simplified "best-fit" impedance model that captures the influence of the complex model without the unnecessary detail. These "best-fit" models help with the characterization of seismic facies, are a means to relate the geology to its seismic properties, and can benefit future studies by improving the computational cost of model simulations (Dadi, 2014 [45]).

I apply the technique described in Dadi et al (2016) [21], to upscale the velocity and density well logs at each of the 7 study locations. The inversion code is performed in a Bayesian framework using a Reverse Jump Markov Chain Monte Carlo (RJMCMC) sampling technique. The RJMCMC varies from other methods in that it preserves both sharp and gradational contacts and uses a transdimensional sampling technique, which treats the number of model layers as an unknown allowing the number of layers to change throughout the inversion. The framework obtains a posterior probability distribution (PPD) of the model parameters using a priori information and a likelihood function (error function):

$$PPD = P(m|d) = \frac{P(d|m)P(m)}{P(d)} \tag{3.2}$$

where,

- d = data used to calculate the likelihood function (synthetic seismogram)
- m = model parameter vectors (k,z,v)
  - z = vector boundary depths
  - v = layer velocity vector
  - k = number of layers (treated as unknown)
- $P(d)$ = probability distribution of all possible models
- $P(d|m)$ = likelihood function (probability of the occurrence of the reference data given the model parameters)
- $P(m)$ = the ppd of $'m'$

The initial data (d) is the synthetic seismogram computed at each location. The likelihood function — $P(d|m)$ — expresses the probability of the occurrence of the reference data given the elastic model and is computed from the squared RMS error between the predicted and reference seismograms (Gibson Hwang, 2009 [44]).

$$P(d|m) = (\frac{1}{2\pi^{\frac{n}{2}}|C_d^{\frac{1}{2}}})exp[-\frac{1}{2}(g(m)-d)^T C_d^{-1}(g(m)-d)] \tag{3.3}$$

where,

- C_d = data covariance error matrix
- $G(m)$ = forward model function representing the synthetic seismogram

I apply the code twice at each location — once using the 30Hz synthetic seismogram as the initial (reference) seismogram, and once using the 60Hz seismogram — for 10000 iterations. At every iteration, a new model is generated by taking one of three possible steps, each with an equal weight in probability: 1) delete a layer, 2) add a layer, 3) move the boundary depths. The code then calculates the acceptance criterion (α) for the new model which is dependent only on the previous model. If $\alpha = 1$, the new model is a better match with the reference seismogram compared than the previous, and the model is accepted. If $\alpha < 1$, the new model is a worse match, and is instead accepted with probability $(1 - \alpha)$. At the completion of the inversion, histograms summarize the models and their chosen layer depths, number of model layers, and squared RMS errors, and the best fit velocity and density impedance models (lowest squared RMS error) are identified.

4. RESULTS

4.1 Generation of Outcrop Logs

The models used to quantify the relationships between rock properties and output velocity and density logs were chosen through trial and error of combining and removing different pools of well data. Before correlating brightness with gamma ray values, a moving average with period 5 was applied to the brightness logs to smooth over fluctuations and better match the gamma ray logs. Well 2 was not included in the pool of data, because the log patterns did not match the trends identified in the other wells which reduced the correlation and regression values. The Scott Ranch well was used to constrain the brightness model results, because it is the one study location with both conventional well logs and a brightness log. The equations for all combinations of data were first applied to the Scott Ranch site, and the extrapolated velocity and density logs were compared to the original well logs. From there, the equations that best reproduced the actual Scott Ranch logs, and had the best correlation and regression parameters, were used to generate velocity and density values at Colonel Neck and Colonel Bend (Table 4.1).

Model No.	**Independent Variable ('X')**	**Dependent Variable ('Y')**	**Well Data Used**	**Corr. Trend**	**Regression Equation**	R^2
1	Brightness	Gamma Ray	Scott Ranch (SR)	Negative (-46.2%)	$Y = 232.91e^{-0.01x}$ (Exponential)	0.3
2	Gamma Ray	Velocity	1, 3, 4	Negative (-63.4%)	$Y = 4.79 - 0.013x$ (Linear)	0.4
3	Gamma Ray	Density	1 & 3	Negative (-58.5%)	$Y = 2.66 - 0.0029x$ (Linear)	0.34
4	Velocity	Density	1, 3, 4	Positive (-64.6%)	$Y = 2.12 + 0.097x$ (Linear)	0.42

Table 4.1: Description of the 4 models calculated using regression techniques to apply to the Lozier Canyon outcrops.

4.2 Synthetic Seismograms & Upscaled Models

Synthetic seismograms using both a 30Hz and 60Hz Ricker wavelet were computed at each location, resulting in 14 total seismograms. Then using the two synthetics as inputs, the RJMCMC upscaling method was applied at each location for 10000 iterations as an input. Ten thousand iterations ensured enough processing time for the convergence to a best fit model with minimum error. For all 14 seismograms, anywhere from 500 to 1900 models were accepted as being a good fit with the forward model.

4.2.1 30Hz Seismograms

The seven synthetic seismograms convolved with a 30Hz Ricker wavelet are shown in Figure 4.1. The time duration of the responses varied between 0.08 seconds (Scott Ranch) and 0.11 seconds (Wells 1 & 4). Maximum peak amplitude occurred in Well 4 at 39 meters, and smallest peak amplitude was Colonel Neck at 14 meters. Vertical resolution of features was calculated for each seismogram using the average velocity values for the Austin Chalk, Eagle Ford, and Buda Limestone and ranges between 31 and 36 meters.

The "best-fit" velocity and density impedance models are defined as the two impedance models that together produce a seismogram with the lowest squared RMS error, compared to all other models, with the reference seismogram. The best fit upscaled models for each well are shown in Figure 4.2 and overlay the initial well logs.The RJMCMC code provides several histogram plots summarizing the results of all 10000 models that describe the depth of layer boundaries, number of layers identified, RMS error, convergence rate and more. Figure 4.3 shows some upscaling results for Well 1, and results for all seven locations are listed in Appendix A. The histogram in Figure (4.3a) plots the depths of identified impedance boundaries versus how many models, out of the 10000 simulated, placed a boundary at that depth. The second histogram (4.3b) illustrates the number of chosen layers versus how many of the iterations modeled that layer number. The final figure (4.3c) plots the RMS squared error for the "best fit model" for each identified layer number. The number of layers that was defined by the most models was not always the number of

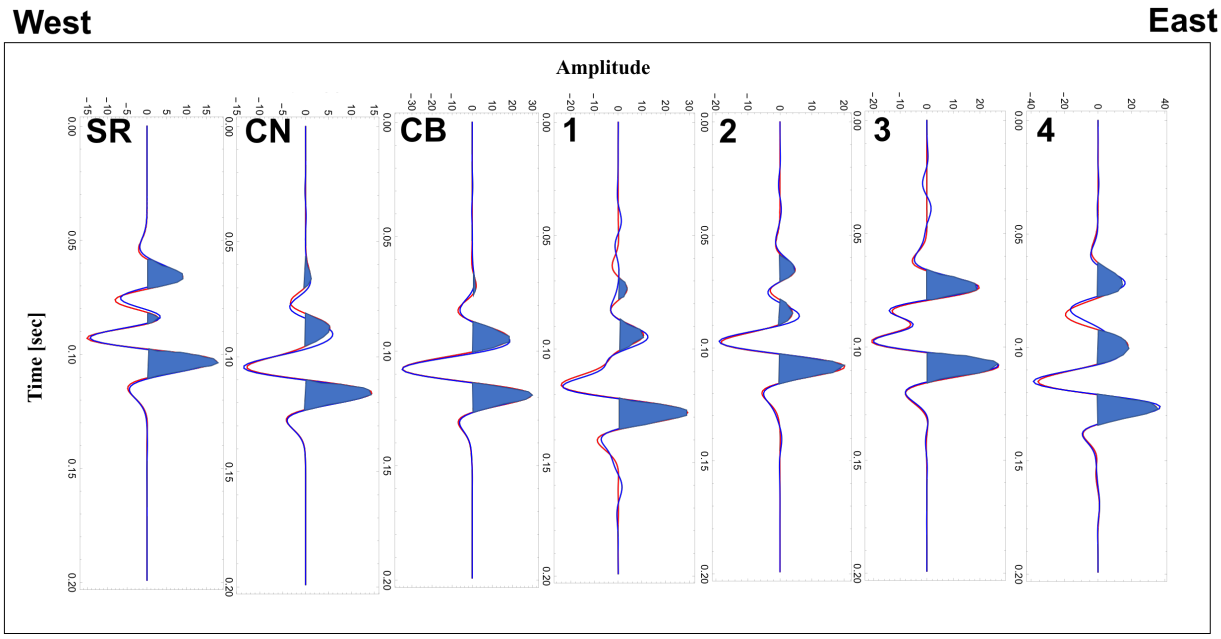

Figure 4.1: Synthetic seismograms for the seven locations convolved with a 30Hz Ricker wavelet. The order of seismograms from left to right mimics the relative location of these sites from west to east (see line in Figure 2.3). Start depth increases from left to right. The red line represents the synthetic seismogram and the blue line is the seismogram produced from the best fit upscaled impedance model.

layers associated with the best fit model. Overall, for the 30Hz seismograms, most of the upscaled models defined 3 layers, but the best fit model with least RMS error averaged 4 layers: the Austin Chalk, Buda Limestone, and two Eagle Ford sections.

4.2.2 60Hz Seismograms

The seismograms computed from the convolution of logs with the 60Hz Ricker wavelet resulted in increased amplitudes, shorter time duration, and a more detailed seismic response compared to the 30Hz wavelets (Figure 4.4). Peak amplitudes ranged from 40 to 60 meters, time duration varied between 0.06 and 0.08 seconds, and resolution of features improved from thicknesses in the mid 30s to between 15 and 17 meters.

The increased detail seen in the synthetic seismograms is paralleled in the upscaled models (Figure 4.5). A greater number of layers were identified by more models at all locations except for

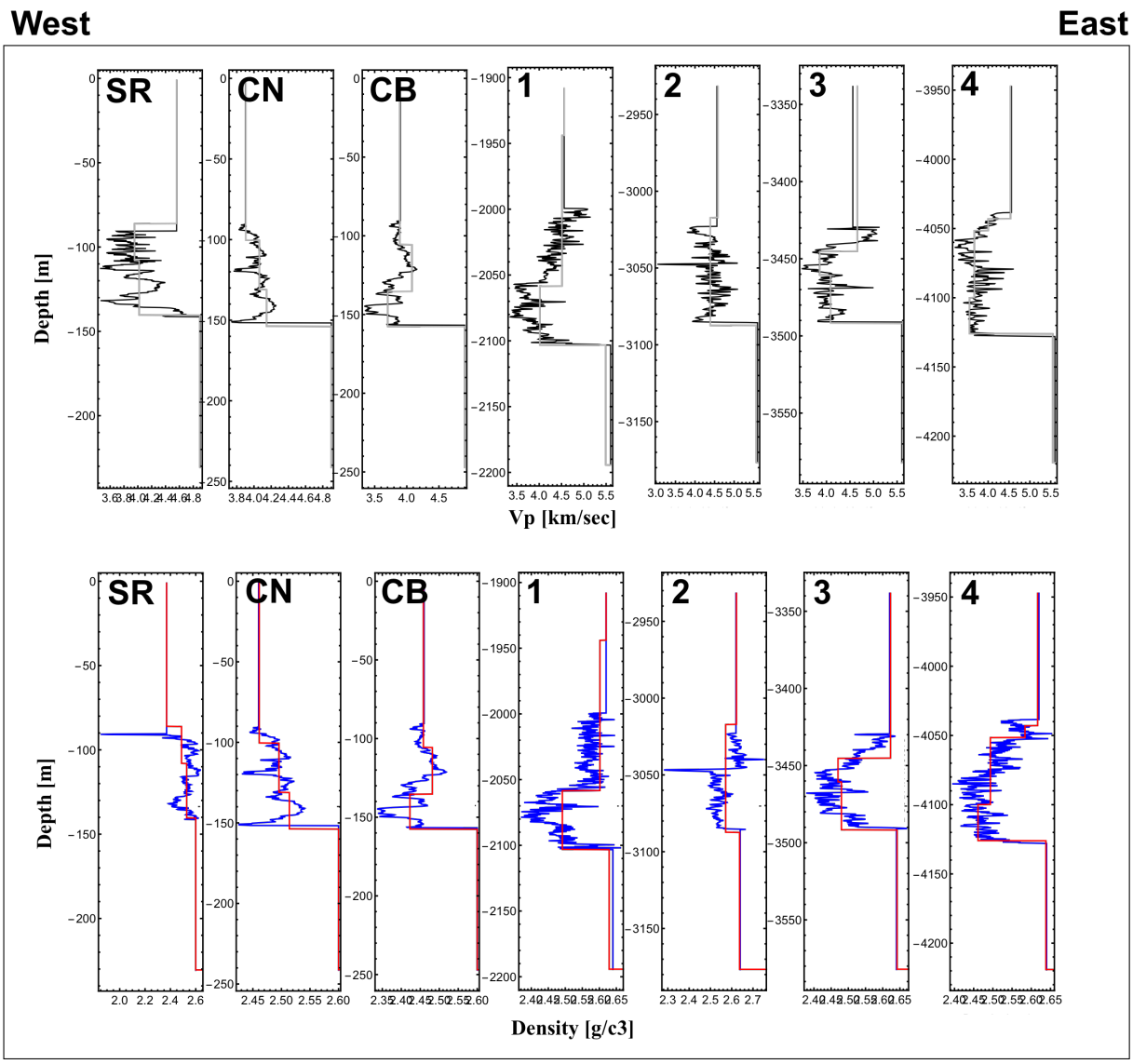

Figure 4.2: "Best-fit" impedance models for the 30Hz seismograms. Models overlay the well log inputs (EF section plus 100 meters of padding on either side). Velocity models are on top and density models are on the bottom.

Colonel Neck and Colonel Bend, which stayed about the same. Overall between 4 or 5 layers were identifies. For Well 1, the most number of models distinguished 5 layers and the best fit model with 7 layers: bottom AC, top Buda, and 5 boundaries within the Eagle Ford.

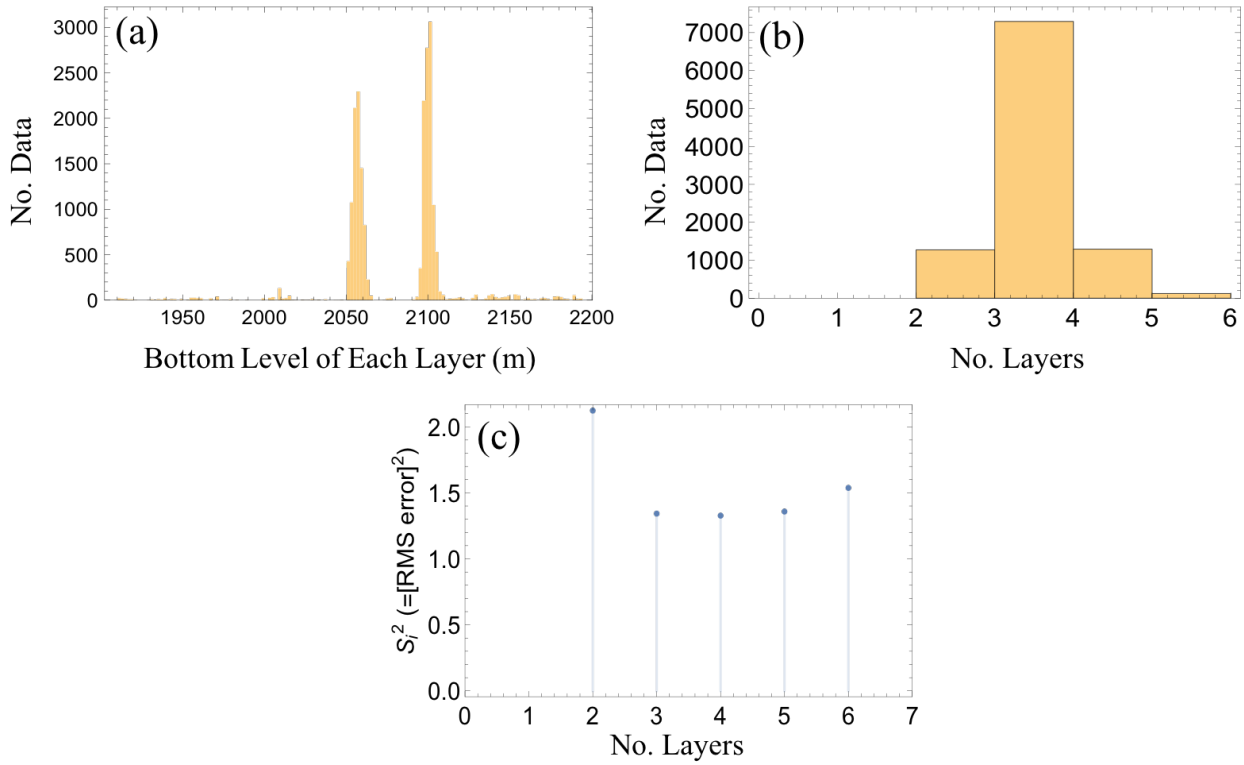

Figure 4.3: A few of the histogram results produced from the RJMCMC upscaling code after 10000 iterations from the 30Hz synthetic seismogram. a) Plots the boundary depths versus how many models interpreted a boundary at that depth. b) Summarizes the 10000 models and how many layers were identified. c) Plots the RMS error of the "best-fit" models for each layer number that was tested.

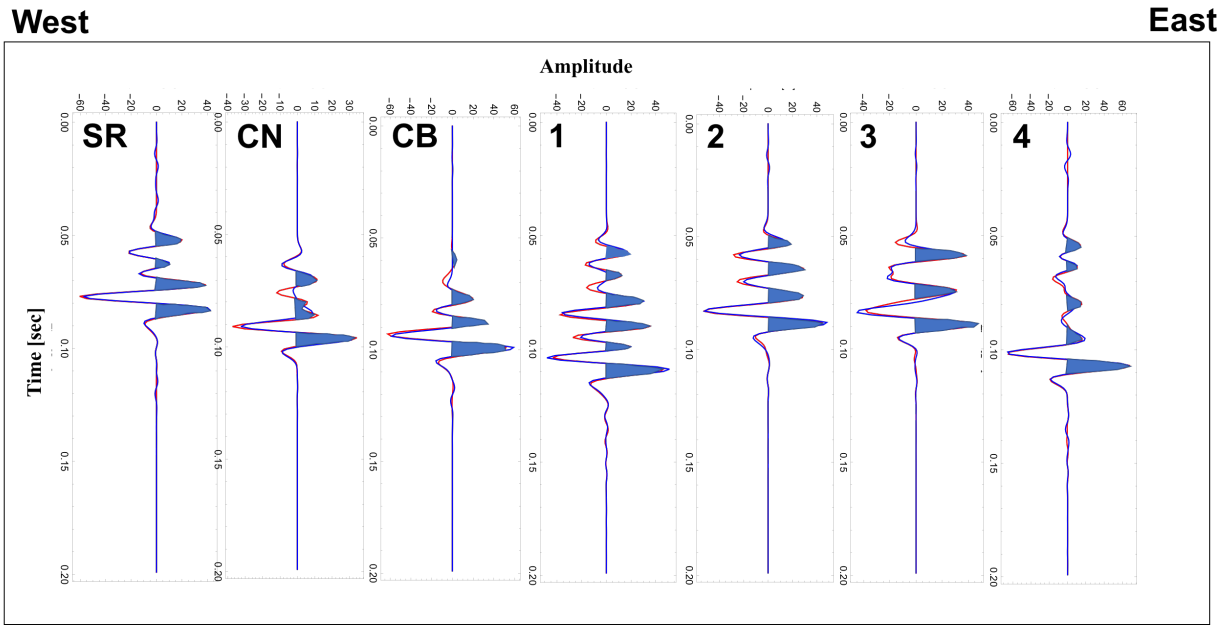

Figure 4.4: Synthetic seismograms for the seven locations convolved with a 60Hz Ricker wavelet. The order of seismograms from left to right mimics the relative location of these sites from west to east (refer to line in Figure 2.3). The red line represents the synthetic seismogram and the blue line is the seismogram produced from the best fit upscaled impedance model.

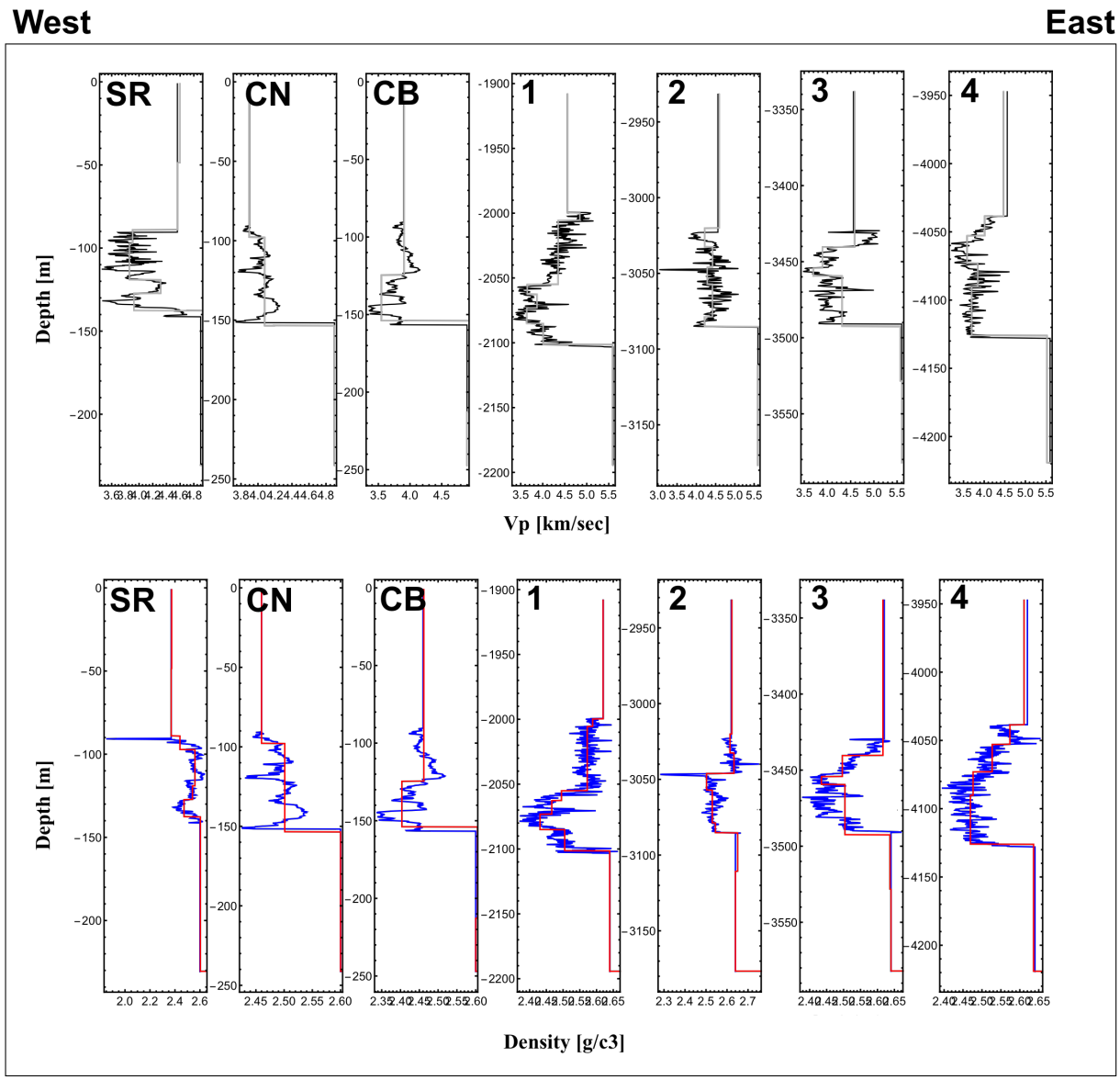

Figure 4.5: "Best-fit" impedance models for the 60Hz seismograms. Models overlay the well log inputs. Velocity models are on top and density models are on the bottom.

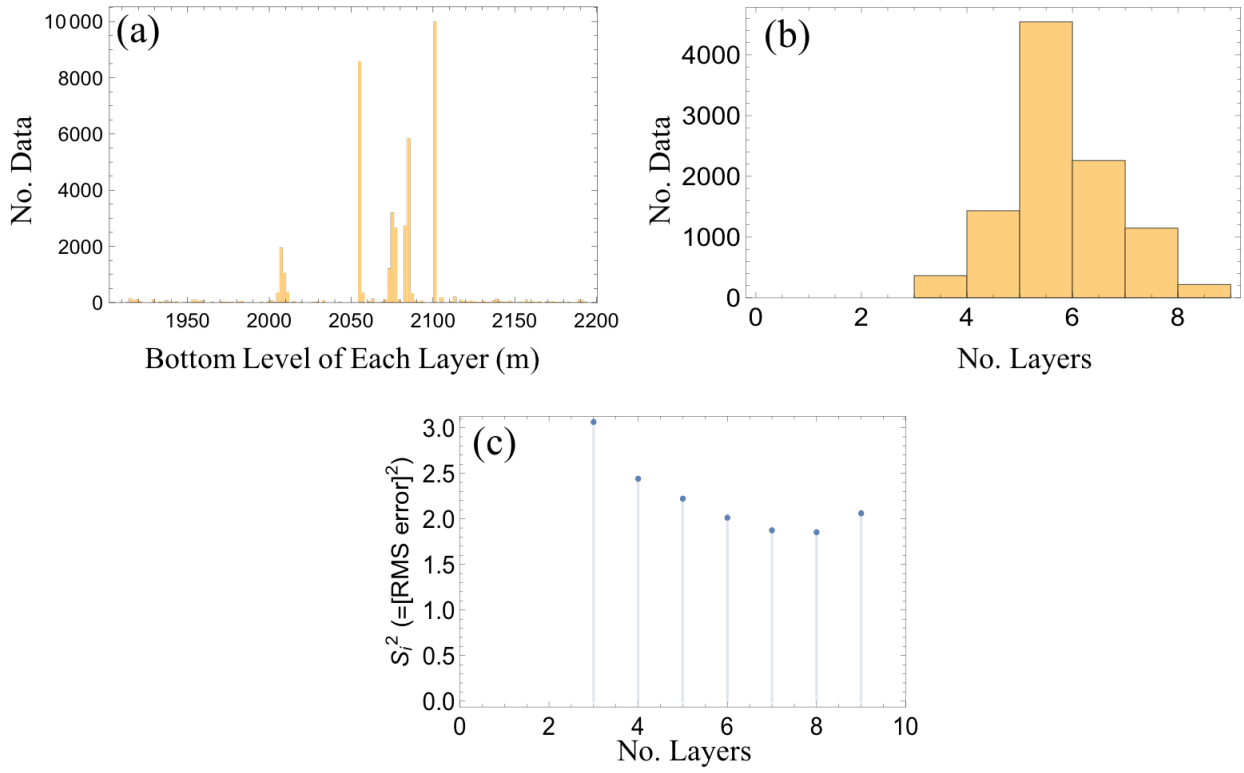

Figure 4.6: A few of the histogram results produced from the RJMCMC upscaling code after 10000 iterations from the 30Hz synthetic seismogram. a) Plots the boundary depths versus how many models interpreted a boundary at that depth. b) Summarizes the 10000 models and how many layers were identified. c) Plots the RMS error of the "best-fit" models for each layer number that was tested.

5. DISCUSSION

5.1 Comparison of Outcrop to Subsurface

5.1.1 Understanding the Outcrop Well Logs

The recorded Scott Ranch velocity log differs from the subsurface logs in that the boundary between facies B and facies C is marked by an increase in values. Geologically a limestone has a higher velocity than a mudstone, so the transition between a limestone interbedded with mudstones (facies C) to an organic rich mudstone interbedded with limestones (facies B) should mark a decrease in velocity, and is observed in the subsurface well logs. It is also interesting to note that the extrapolated velocity log at Colonel Neck modeled from the brightness, recorded an increase in velocity as well (Appendix B — Figure B.2), which infers a change in the geology within facies B. This abnormal increase could potentially be explained by weathering to the outcrop, diagenesis to the rock, cementation, or fundamentally a difference in rock properties based on its original depositional location. Anselmetti and Eberli (2012) [47] researched that diagenesis and cementation have an affect on large ranges in velocities of carbonates at shallow depths.

Other observed differences between the extrapolated logs at Colonel Neck and Colonel Bend with the well logs acquired through conventional logging techniques, were the lack of diversity and overall lower values of the velocity and density logs. The lack of diversity can be explained by the regression models used, because the equations were based on the average values of the petrophysical relationships, which eliminated naturally occurring variation. The use of averages still identifies similar impedance trends between layers, but limits the contrast at the boundaries, affecting the seismic amplitudes, which is conveyed at the Colonel Neck site (Figure 4.1). The lower values could be a by-product of the petrophysical relationships that defined the regression models. Brightness logs are proxy data and do not directly measure geological data. Instead the values measure the average color values along a composite section taken from 2D photogrammetry. Therefore, irregular lighting, debris, weathered rocks, or where along the section a measurement

is taken, are all possibilities for an inaccurate representation of the geology and thus result in a decrease correlation between brightness and gamma ray.

In future studies beyond the scope of this project, improvement in the methodology of how brightness logs are calculated, along with the development of a more complex model that incorporates a random distribution of values from the average measurements and is constrained by the variance, could improve well log extrapolations.

5.1.2 Comparison Between Outcrops and Subsurface

Knowledge of the Eagle Ford outcrops can enhance the predictability of the spatial distribution and characterization of facies in the subsurface (Davis, 2017 [3]; Workman, 2013 [4]). Overall, the seismic responses for the Lozier Canyon outcrops most closely exhibit the response patterns observed at Wells 2 and 4 for the 30Hz seismograms and Wells 2 and 3 for the 60Hz seismograms (Figures 4.1 and 4.4). Wells 2 and 3 have similar total Eagle Ford thicknesses with the outcrops, and Well 2 most closely resembled the log patterns. The seismic amplitudes displayed at Scott Ranch and Colonel Neck were smaller compared to the amplitudes observed at the subsurface.

5.2 Changes in seismograms related to changes in facies

5.2.1 Log Impedance Models vs. Best-Fit Upscaled Models

Estimating both the forward and inverse model creates a bridge between high frequency log data and lower frequency seismic, allowing for more insight into how the geophysical data relates to the physical geology (Dadi et al, 2016 [21]; Dileep et al, 2009 [48]). The upscaled models were therefore a means to be able to test for which facies, or "layers", are represented on the seismograms and compare those boundaries to the actual facies boundaries identified by other logs. Figure 5.1 illustrates 3 different interpretations shown for Well 1: 1) interpretation of facies boundaries based on log patterns, 2) interpretation of 30Hz upscaled "best fit" model, and 3) interpretation of 60Hz upscaled "best fit" model. All other comparisons between the models for the locations are referenced in Appendix B. Table 5.1 lists the number of models that identified the correct boundary based on the original interpretation for the 30Hz and 60Hz wavelets and defines the total

percentage of models that correctly identified the boundaries.

Boundary:	**No. Locations Identified (30Hz):**	**No. Locations Identified (60Hz):**	**Percentage Identified (Total)**
AC-EF	2	5	50%
E-D	1	1	14%
D-C	2	3	36%
C-B	2	6	57%
B-A	0	0	0%
EF-Buda	7	7	100%

Table 5.1: Summary of the number of models that correctly identified the facies boundaries or the 30Hz and 60Hz wavelets. Total percentage identified is the percentage of models (out of 14) that identified the labeled facies.

The Eagle Ford — Buda contact was consistently identified for all best fit models. The next boundary identified the most is the C-B contact which separates the Upper from the Lower Eagle Ford, followed by the Austin Chalk (AC) — EF contact, and the D-C contact. The similar velocity and density log properties for Facies D and E at the subsurface well locations, coupled with their small thicknesses, made the boundary between the two difficult to identify even with the aid of other well logs, and the facies boundary was not identified on any upscaled models for the subsurface locations, but were distinguished at the outcrops. On the contrary, the boundary between facies B and C, or the separation between the Upper Eagle Ford and Lower Eagle Ford, overall has distinct change in log character marked by a decrease in velocity and density with the change in geology that is picked up on 8 out of the 14 upscaled models.

The best-fit upscaled model results may define impedance boundaries that re-create the synthetic seismograms with low RMS errors, but it is important to keep in mind the geology to know which models add geologic value and which models are not geologically feasible. Some of the models for the 30Hz seismograms, particularly the outcrop locations and Well 3, identify boundaries that do not align with the geology, and are placed to match the reference seismogram. While,

the increased detail of the 60Hz seismograms identify more of the facies boundaries, but also include additional boundaries in Facies B that geologically do not add value, but increase the match between the reference and upscaled seismogram.

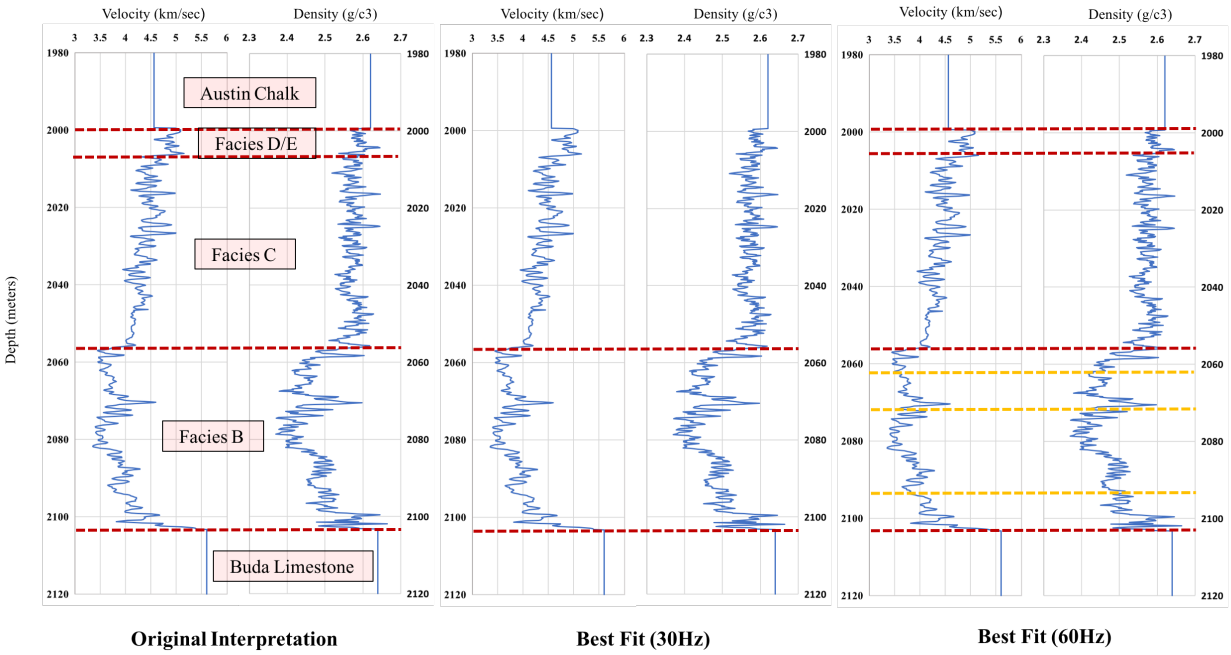

Figure 5.1: Velocity and Density well logs for Well 1. Logs include recorded Eagle For values in between averaged constant values representative of the Austin Chalk and Eagle Ford. The "Original Interpretation" (left) marks the layer boundaries determined by log patterns including logs not shown such as gamma ray, resistivity, etc. The middle marks the boundaries determined by the best fit model — lowest RMS error — for the 30Hz synthetic seismogram and the right logs mark the boundaries for the best fit 60Hz model. The layers labeled in orange are those layers identified by the best fit model but do not represent any of the facies layers.

5.2.2 Seismogram Interpretation of Facies Boundaries

Three layer boundaries were mapped on the seismograms (Figures 5.2 and 5.3): the top of the Eagle Ford, Facies C — B contact, and the bottom of the Eagle Ford. The EF-Buda boundary is marked by a peak at the end of the signal on both the 30Hz and 60Hz seismograms. The increase in impedance of the Eagle Ford into the Buda is more pronounced than the other boundaries results

in the highest amplitudes in the seismogram and a consistent presence across all seven locations. Research from Christensen and Szymanski (1991) [46] validated this observation by noting that shales in contact with carbonates produce maximum amplitude reflections.

The C-B contact was mapped on a trough which mirrored the decrease in velocity and density from the Upper Eagle Ford to the Lower Eagle Ford, but which trough the contact was mapped on varied between the seven locations. For the 30Hz seismograms, the trough was contiguous with the EF-Buda peak below with the exceptions of Wells 3 and 4, and on the 60Hz seismograms, the contact was mapped on the trough second from the bottom with exceptions of Wells 1, 4, and Scott Ranch. Where the C-B boundary was placed was dependent on the internal distribution of facies. Wells 3 and 4 contain the highest ratio of Facies B compared to the Upper Eagle Ford facies at around 70% and 80%. The Eagle Ford response at Wells 3 and 4 will therefore be predominantly representative of Facies B, shifting the boundary up earlier on the seismogram. The boundary placement at Well 1 differs, because it contains the thickest Eagle Ford section, and when the logs were convolved with the 60Hz wavelet, the increased resolution resulted in a longer response time with more cycles than the other locations. The more detailed response coupled with roughly a 50/50 ratio between the Upper Eagle Ford and Lower Eagle Ford facies distribution, defined the C-B boundary on a different trough than the other seismograms. The interpretation for the Scott Ranch location was different, because the C-B boundary was placed on a peak rather than a trough. This addresses the difference in well log patterns from the other wells with the increase in velocity at the boundary resulting in an increase in impedance.

The last boundary interpreted on the seismograms was the AC-EF contact, which has previously been described as a gradational contact, because of the similar lithologies (Hammes et al, 2016 [1]). For the seven locations in this study, the overall trend was a negative impedance contrast between the average Austin Chalk values and underlying Eagle Ford, mapping the boundary on a trough. Well 3 was the only location that was mapped on a peak and I believe the contradiction was manifested by the simplification of Austin Chalk log values in the model. The average values of the Austin Chalk were lower than the actual Eagle Ford values, creating a positive impedance

contrast.

The other facies contacts in the Upper Eagle Ford were not mapped on the synthetic responses, because their individual thicknesses were beneath the resolution limit at both 30Hz and 60Hz frequencies, and therefore could not confidently be picked across the seismograms. The thicknesses of Facies B are only sometimes above tuning for 30Hz frequencies, but is resolvable when using 60Hz (for thicknesses, refer to Table 3.1). The boundaries for the Upper Eagle Ford facies may not be resolved as individual features, but their impedance contrasts affect the shape and amplitudes of the seismogram response through constructive and destructive interference. The interference could play a role in why some of the wells have peak "responses" (Scott Ranch, Well 2, and Well 4) above the trough mapped as the AC-EF boundary along with the fundamental shape of a Ricker wavelet.

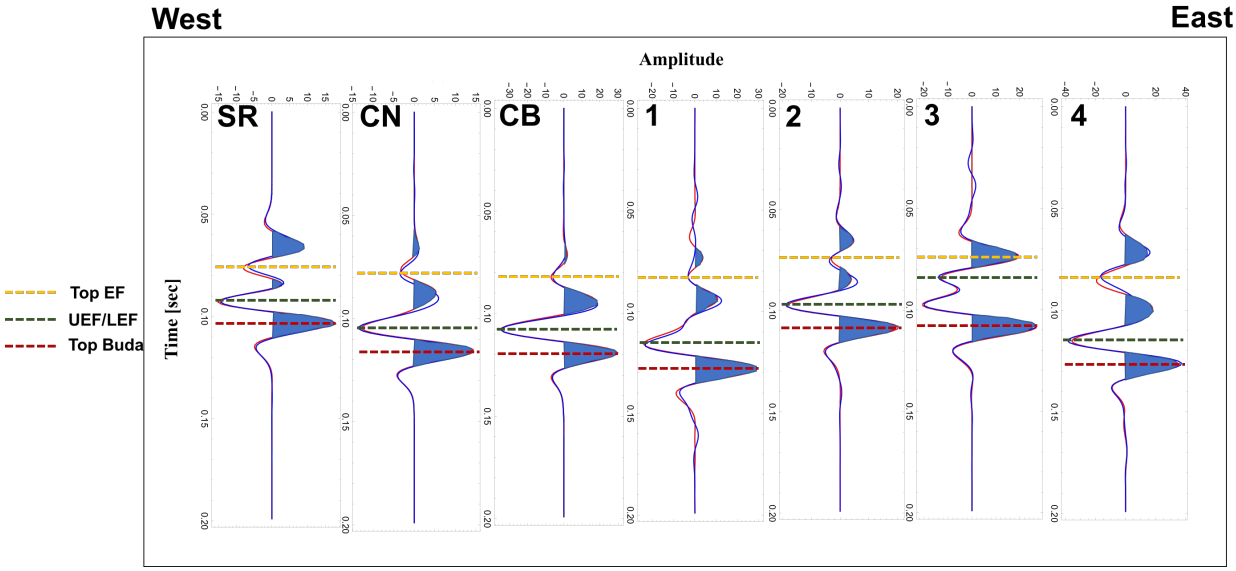

Figure 5.2: Three facies boundaries mapped on the 30Hz synthetic seismograms (red) and seismograms computed from the best-fit models (blue).

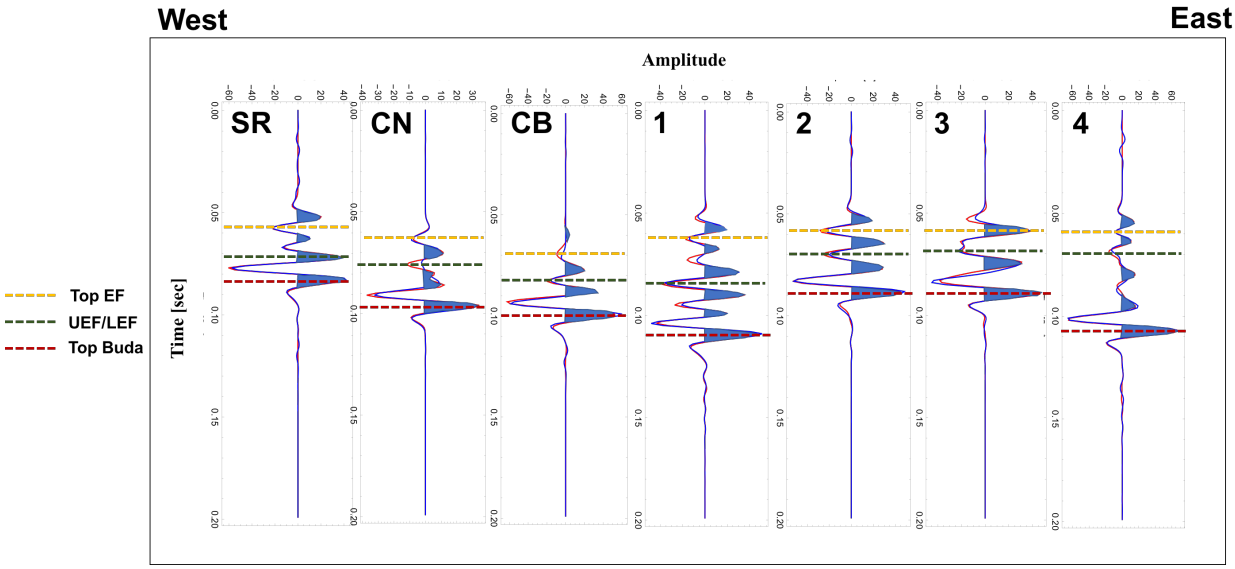

Figure 5.3: Three facies boundaries mapped on the 60Hz synthetic seismograms (red) and seismograms computed from the best-fit models (blue).

6. CONCLUSION

Modeled outcrop logs using brightness logs as gamma ray logs are successful in modeling synthetic seismograms with similar character responses compared to other regional Eagle Ford locations, but are limited in the amount of variation of log values. Outcrop responses most closely match the subsurface well locations with similar thicknesses and the well log patterns at Scott Ranch and Colonel Neck exhibit an increase in velocity values where a decrease is expected. Upscaled models confirm log patterns linked to facies changes within the Eagle Ford. As the frequency of the data increases, resolution doubles, revealing more detail of facies boundaries seen in both the seismograms and upscaled impedance models. Correct identification of boundaries in the best-fit models increased from 29% to 71% for the AC-EF, 29% to 43% for the D-C boundary, and 29% to 86% for the C-B boundary, between 30Hz and 60Hz frequencies. Overall, the only facies boundary within the Eagle Ford that could be repeatably identified at all seven locations was the C-B boundary (Upper Eagle Ford - Lower Eagle Ford). Facies C, D, and E are individually beneath the seismic resolvability for both applied frequencies (30Hz and 60Hz), inferring that their presence effects the response through either constructive or destructive interference. The number of cycles within the synthetic seismograms vary between locations because of differences in total Eagle Ford thicknesses. Therefore, where the C-B contact is mapped changes across the region and is dependent on the facies distribution and thickness ratios between the facies.

REFERENCES

[1] U. Hammes, R. Eastwood, G. McDaid, E. Vankov, A. S. Gherabati, K. Smye, J. Shultz, E. Potter, S. Ikonnikova, and S. Tinker, "Regional assessment of the Eagle Ford Group of south Texas, USA: Insights from lithology, pore volume, water saturation, organic richness, and productivity correlations," *Interpretation*, vol. 4, pp. SC125–SC150, 2016.

[2] A. D. Donovan and T. S. Staerker, "Sequence stratigraphy of the Eagle Ford (Boquillas) Formation in the subsurface of south Texas and the outcrops of west Texas," *Transactions - Gulf Coast Association of Geologic Societies*, vol. 60, pp. 861–899, 2010.

[3] D. E. Davis, "Digital outcrop models of the Eagle Ford Group in Lozier Canyon, Terrell County, Texas," Master's thesis, Texas AM University, 2017.

[4] S. J. Workman, "Integrating depositional facies and sequence stratigraphy in characterizing unconventional reservoirs: Eagle Ford Shale, south Texas," Master's thesis, Western Michigan University, 2013. p. 141.

[5] B. of Economic Geology, "Geologic Map of Texas," 1992. The University of Texas at Austin.

[6] A. D. Donovan, T. S. Staerker, A. Pramudito, W. Li, M. J. Corbett, C. M. Lowery, A. M. Romero, and R. D. Gardner, "The Eagle Ford outcrops of west Texas: A laboratory for understanding heterogeneities within unconventional mudstone reservoirs," *Gulf Coast Association of Geologic Societies Journal*, vol. 1, pp. 162–185, 2012.

[7] A. D. Donovan, S. Staerker, R. D. Gardner, M. C. Pope, A. Pramudito, and M. P. Wehner, "Findings from the Eagle Ford outcrops of west Texas and implications to the subsurface of south Texas," *American Association of Petroleum Geologists, ed., The Eagle Ford Shale: A renaissance in U.S. oil production*, vol. AAPG Memoir 110, pp. 301–336, 2016.

[8] Q. Ren, *Anisotropic seismic characterization of the Eagle Ford Shale: Rock-physics modeling, stochastic seismic inversion, and geostatistics*. PhD thesis, The University of Texas at

Austin, 2016.

[9] W. C. Dawson, "Shale microfacies: Eagle Ford Group (Cenomanian-Turonian) North-Central Texas outcrops and subsurface equivalents," *Gulf Coast Association of Geological Societies Transactions*, pp. 607–622, 2000.

[10] N. Basu, G. Barzola, H. Bello, P. Clarke, and O. Viloria, "Eagle Ford reservoir characterization from multisource data integration," *Search and Discovery*, no. 80234, 2012. Annual Convention and Exhibition, AAPG, Abstract.

[11] J. A. Breyer, R. Denne, J. Funk, T. Kosanke, and J. Spaw, "Stratigraphy and sedimentary facies of the Eagle Ford Shale (Cretaceous) between the Maverick Basin and the San Marcos Arch, Texas, USA," *Search and Discovery article*, no. 50899, 2013.

[12] S. J. Workman and G. M. Grammer, "Integrating depositional facies and sequence stratigraphy in characterizing unconventional reservoirs in the Cretaceous (Cenomanian-Turonian) Eagle Ford Shale, south Texas," *Gulf Coast Association of Geological Societies Transactions*, vol. 63, pp. 473–508, 2013.

[13] B. Tinnin, H. Bello, and M. McChesney, "Multi-source data integration to predict well performance: Eagle Ford sweet spot mapping," *AAPG Search and Discovery*, no. 41397, 2014. AAPG Abstract.

[14] J. A. Breyer, "Limestone frequency and well performance, Eagle Ford Shale (Cretaceous), South Texas." GTW presentation, 2015.

[15] T. F. Hentz and S. C. Ruppel, "Regional lithostratigraphy of the Eagle Ford Shale: Maverick Basin to East Texas Basin," *Transactions of the Gulf Coast Association of Geological Societies*, vol. 60, pp. 225–337, 2010.

[16] B. Matsutsuyu, "South Texas Eagle Ford Shale geology — Regional trends, recent learnings, future challenges." Presented at the AAPG-DUG Conference, 2011.

[17] O. Ogiesoba and U. Hammes, "Seismic-attribute identification of brittle and TOC-rich zones within the Eagle Ford Shale, Dimmit County, South Texas," *Journal of Petroleum Exploration and Production Technology*, vol. 4, pp. 133–151, 2014.

[18] G. Treadgold, S. Sinclair, D. F. Nicklin, and B. Campbell, "Eagle Ford Shale prospecting with 3-D seismic data within a tectonic and depositional system framework," *The Leading Edge*, vol. 30, pp. 48–53, 2011.

[19] P. Santogrossi, "Sub-seismic resolution in the Eagle Ford enabled by multi- attribute analysis in paradise: Instantaneous, geometric, and spectral decomposition self-organizing maps (SOMs)," *SEG Convention*, 2015.

[20] B. Chen, D. Kumar, A. Uerling, S. Land, O. Aguirre, T. Jian, and S. Sugianto, "Seismic inversion and net pay to calibrate Eagle Ford Shale producible resources," *Search and Discovery*, vol. 00104, 2016. GCAGS, Presentation.

[21] S. Dadi, R. Gibson, and K. Wang, "Velocity log upscaling based on reversible jump Markov chain Monte Carlo Simulated Annealing," *Geophysics*, vol. 81, no. 5, pp. R293–R305, 2016.

[22] R. D. Gardner, M. C. Pope, M. P. Wehner, and A. D. Donovan, "Comparative stratigraphy of the Eagle Ford Group strata in Lozier Canyon and Antonio Creek, Terrell County, Texas," *Transactions- Gulf Coast Association of Geological Societies*, vol. 63, pp. 673–674, 2013.

[23] R. T. Hazzard, *Measured Section, in Geology of the Val Verde Basin, West Texas Geological Society Guidebook*. 1959. p. 118.

[24] V. L. Freeman, "Contact of the Boquillas Flags and Austin Chalk in Val Verde and Terrell counties, Texas," *American Association of Petroleum Geologists Bulletin*, vol. 45, pp. 105–107, 1961.

[25] V. L. Freeman, "Geology of the Comstock-Indian wells area Val Verde, Terrell, and Brewster counties, Texas," *U.S. Geological Survey Professional Paper*, no. 594-K, p. 263, 1968.

[26] R. H. Trevino, "Facies and depositional environments of the Boquillas Formation, Upper Cretaceous of southwest Texas," Master's thesis, University of Texas at Arlington, 1988. p. 135.

[27] E. A. Pessagno, "Upper Cretaceous stratigraphy of the western gulf coast area of Mexico, Texas, and Arkansas," *Geological Society of America Memoirs*, vol. 111, pp. 1–139, 1969.

[28] B. E. Lock and L. S. Peschier, "Boquillas (Eagle Ford) upper slope sediments, West Texas: Outcrop analogs for potential shale reservoirs," *Gulf Coast Association of Geologic Societies Transactions*, vol. 56, pp. 491–508, 2006.

[29] A. D. Donovan, R. D. Gardner, A. Pramudito, T. S. Staerker, M. Wehner, M. J. Corbett, J. J. Lundquist, A. M. Romero, L. C. Henry, J. R. Rotzien, and K. S. Boling, "Chronostratigraphic relationships of the Woodbine and Eagle Ford Groups across Texas," *Gulf Coast Association of Geologic Societies Journal*, vol. 4, pp. 67–87, 2015.

[30] M. Wehner, M. M. Tice, M. C. Pope, R. Gardner, A. D. Donovan, and T. S. Staerker, "Anoxic, storm dominated inner carbonate ramp deposition of lower Eagle Ford Formation, west Texas," *Society of Petroleum Engineers*, 2015.

[31] E. J. Barron and W. M. Washington, "The role of geographic variables in explaining paleoclimates: Results from Cretaceous climate model sensitivity studies," *Journal of Geophysical Research: Atmospheres*, vol. 89, no. D1, pp. 1267–1279, 1984.

[32] R. T. Hill, "The Texas section of the American Cretaceous," *American Journal of Science*, vol. 34, pp. 287–309, 1987.

[33] P. A. Scholle, D. G. Bebout, and C. H. Moore, "Carbonate depositional environments, Tulsa, OK," *AAPG Memoir*, 1983.

[34] B. S. Hart, "The Greenhorn cyclothem of the Cretaceous Western Interior Seaway: Lithology trends, stacking patterns, log signatures, and application to the Eagle Ford of west Texas," *Gulf Coast Association of Geologic Societies Transactions*, vol. 65, pp. 155–174, 2015.

[35] A. D. Donovan, T. S. Staerker, A. Pramudito, R. D. Gardner, M. C. Pope, M. J. Corbett, C. M. Lowery, and A. M. Romero, "A 3D outcrop perspective of an unconventional carbonate mudstone reservoir." URTeC 1580954, Denver, Colorado, August 12–14 2013.

[36] R. K. Goldhammer and C. A. Johnson, "Middle Jurassic — Upper Cretaceous paleogeographic evolution and sequencestratigraphic framework of the northwest Gulf of Mexico Rim, in C. Bartolini, R. T. Buffler, and A. Cantu-Chapa, eds., the western Gulf of Mexico Basin: Tectonics, sedimentary basins," *American Association of Petroleum Geologists Memoir*, vol. 75, pp. 45–81, 1999.

[37] T. E. Ewing, "Review of late Jurassic depositional systems and potential hydrocarbon plays, northern Gulf of Mexico Basin," *Gulf Coast Association of Geological Societies Transactions*, vol. 51, pp. 85–96, 2001.

[38] R. K. Goldhammer and C. A. Johnson, "Middle Jurassic — Upper Cretaceous paleogeographic evolution and sequence-stratigraphic framework of the northwest Gulf of Mexico Rim, in C. Bartolini, R. T. Buffler, and A. Cantu-Chapa, eds., the western Gulf of Mexico Basin," *AAPG Memoir*, vol. 75, pp. 45–81, 2001.

[39] J. S. Birch, "Using 3DM analyst mine mapping suite for rock face characterisation, in Tonon, F., and Kottenstette, J. T., eds.," *The 41st U.S. Rock Mechanics Symposium, Laser and Photogrammetric Methods for Rock Face Characterization*, pp. 13–32, 2006. American Rock Mechanics Association.

[40] S. P. Bemis, S. Micklethwaite, D. Turner, M. R. James, S. Akciz, S. T. Thiele, and H. A. Bangash, "Ground-based and UAV-Based photogrammetry: A multi-scale high-resolution mapping tool for structural geology and paleoseismology," *Journal of Structural Geology*, vol. 69, pp. 163–178, 2014.

[41] W. L. Russell, "Relation of radioactivity, organic content, and sedimentation," *American Association of Petroleum Geologists Bulletin*, vol. 29, no. 10, pp. 1470–1494, 1945.

[42] R. P. McNeal, "Lithologic analysis of sedimentary rocks," *American Association of Petroleum Geologists Bulletin*, vol. 43, no. 4, pp. 854–879, 1959.

[43] K. H. Zou, K. Tuncali, and S. G. Silverman, "Correlation and simple linear regression," *Radiology*, vol. 227, pp. 617–628, 2003.

[44] R. L. Gibson and K. L. Hwang, "Quantification of uncertainty in velocity log upscaling by a Markov Chain Monte Carlo method," 2009. SEG Annual Meeting.

[45] S. K. Dadi, *Estimation of Impedance Using Seismic Reflection Data Based on Transdimensional Inversion*. PhD thesis, Texas AM University, 2014.

[46] N. I. Christensen and L. Szymanski, D., "Seismic properties and the origin of reflectivity from a classic Paleozoic sedimentary sequence, valley and ridge province, southern Appalachians," *Geological Society of America Bulletin*, vol. 103, pp. 277–289, 1991.

[47] F. S. Anselmetti and G. P. Eberli, "Sonic velocity in carbonates — A combined product of depositional lithology and diagenetic alterations society for sedimentary geology special publication," *Society for Sedimentary Geology Special Publication*, no. 70, pp. 193–216, 2001.

[48] T. K. Dileep, I. O. Bayuk, A. A. Vikhorev, and E. M. Chesnokov, "Comparison of seismic upscaling methods: From sonic to seismic," *Geophysics*, vol. 74, no. 2, pp. WA3–WA14, 2009.

APPENDIX A

Upscaling results for the seven study locations. Figures are listed in order of occurrence in Figure 2.3 from left to right.

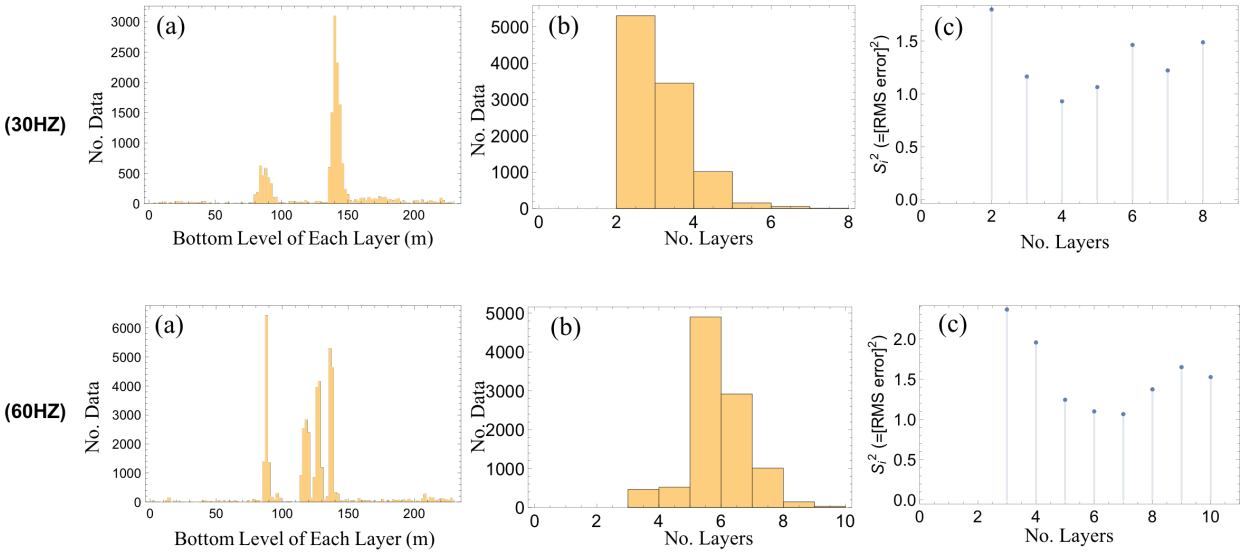

Figure A.1: Upscaling plots for Scott Ranch. 30Hz (top) and 60Hz (bottom)

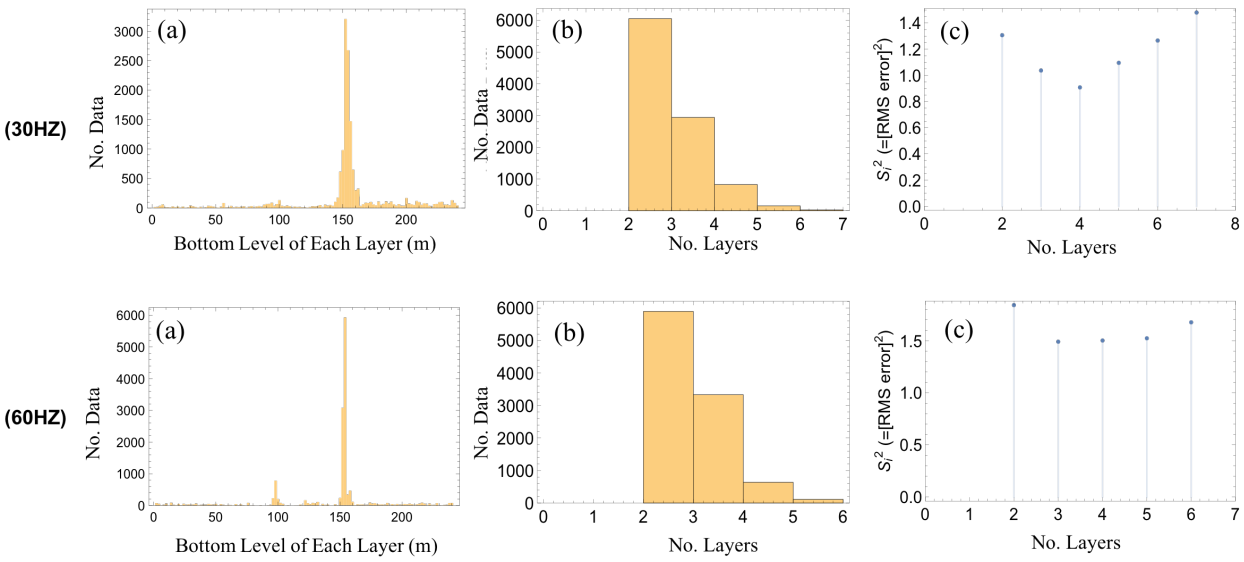

Figure A.2: Upscaling plots for Colonel Neck. 30Hz (top) and 60Hz (bottom)

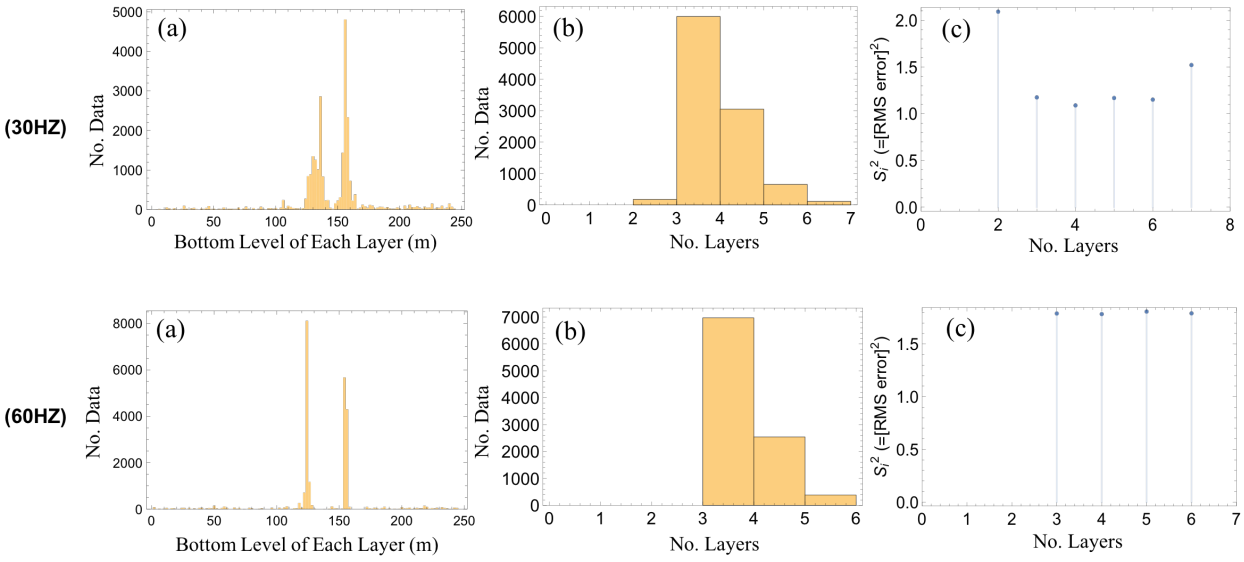

Figure A.3: Upscaling plots for Colonel Bend. 30Hz (top) and 60Hz (bottom)

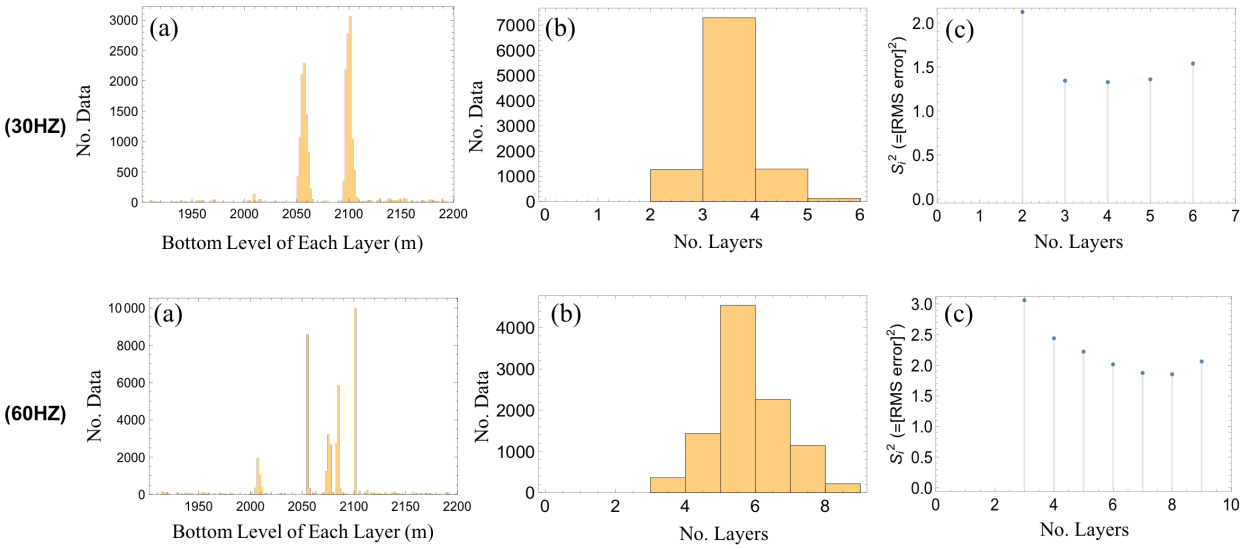

Figure A.4: Upscaling plots for Well 1. 30Hz (top) and 60Hz (bottom)

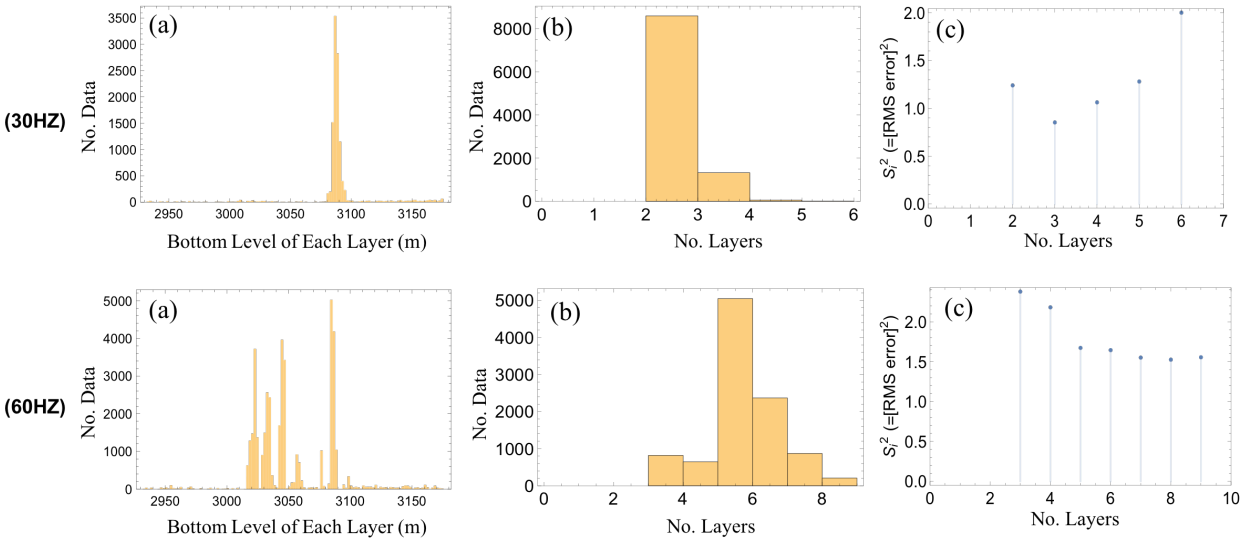

Figure A.5: Upscaling plots for Well 2. 30Hz (top) and 60Hz (bottom)

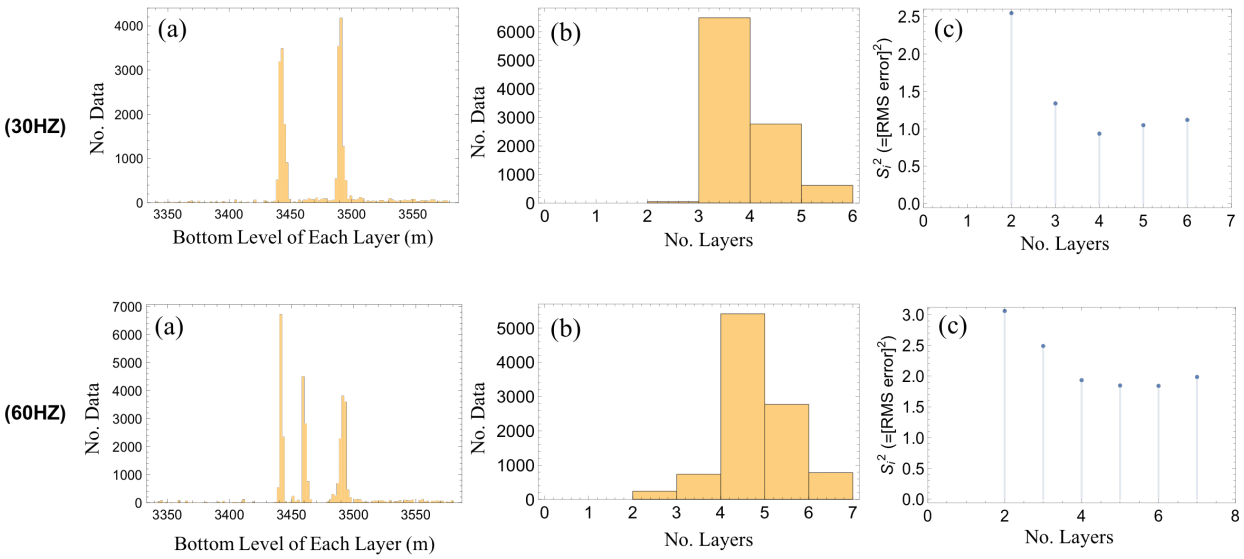

Figure A.6: Upscaling plots for Well 3. 30Hz (top) and 60Hz (bottom)

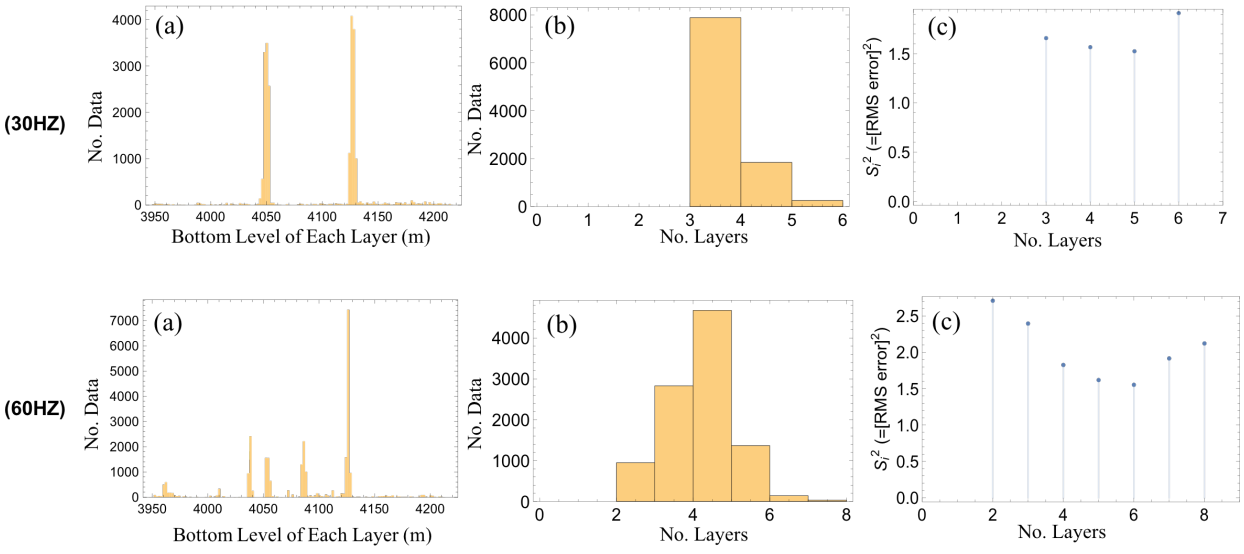

Figure A.7: Upscaling plots for Well 4. 30Hz (top) and 60Hz (bottom)

APPENDIX B

Listed below are the identified facies boundaries of the well log interpretations compared with the upscaled results of the 30Hz and 60Hz seismograms for the seven study locations. Figures are listed in order of occurrence in Figure 2.3 from left to right.

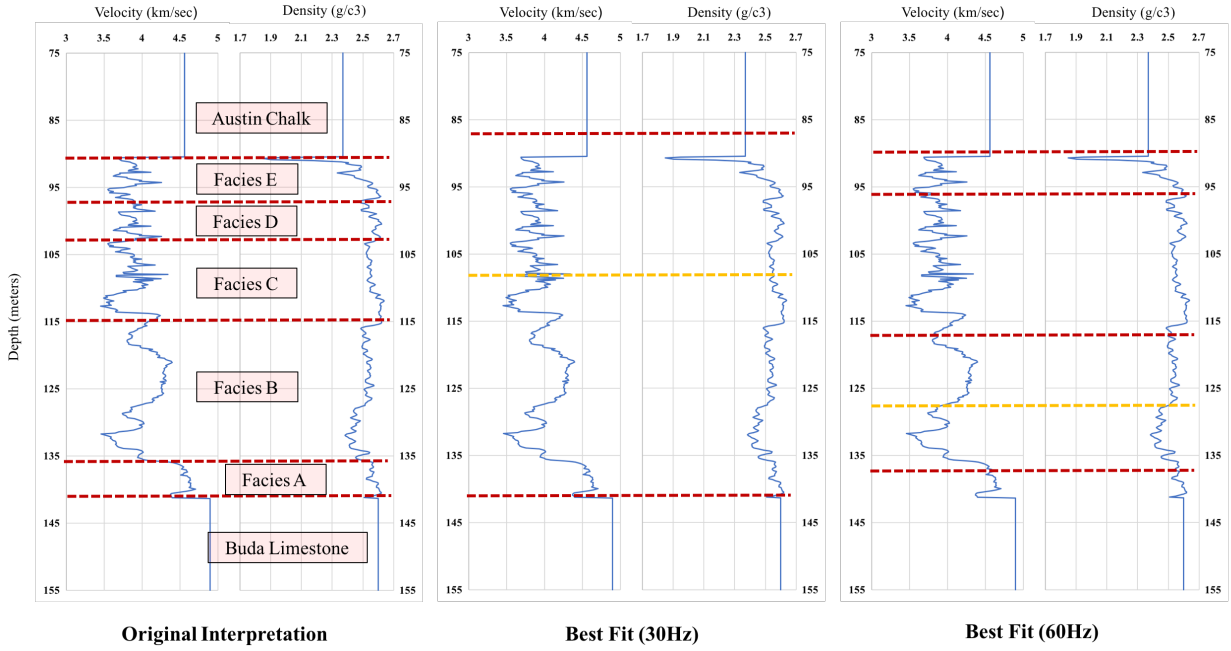

Figure B.1: Comparison of facies interpretation at Scott Ranch between original log interpretation (left), 30Hz best-fit upscaled model (center), and 60Hz best-fit upscaled model (right).

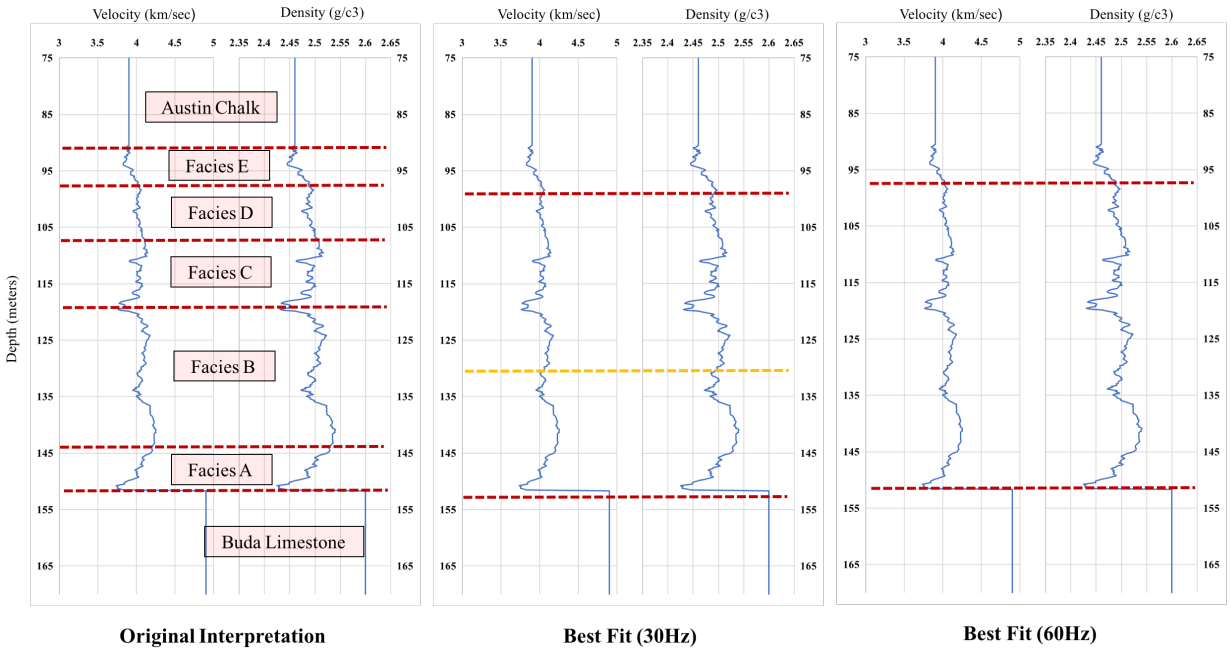

Figure B.2: Comparison of facies interpretation at Colonel Neck between original log interpretation (left), 30Hz best-fit upscaled model (center), and 60Hz best-fit upscaled model (right).

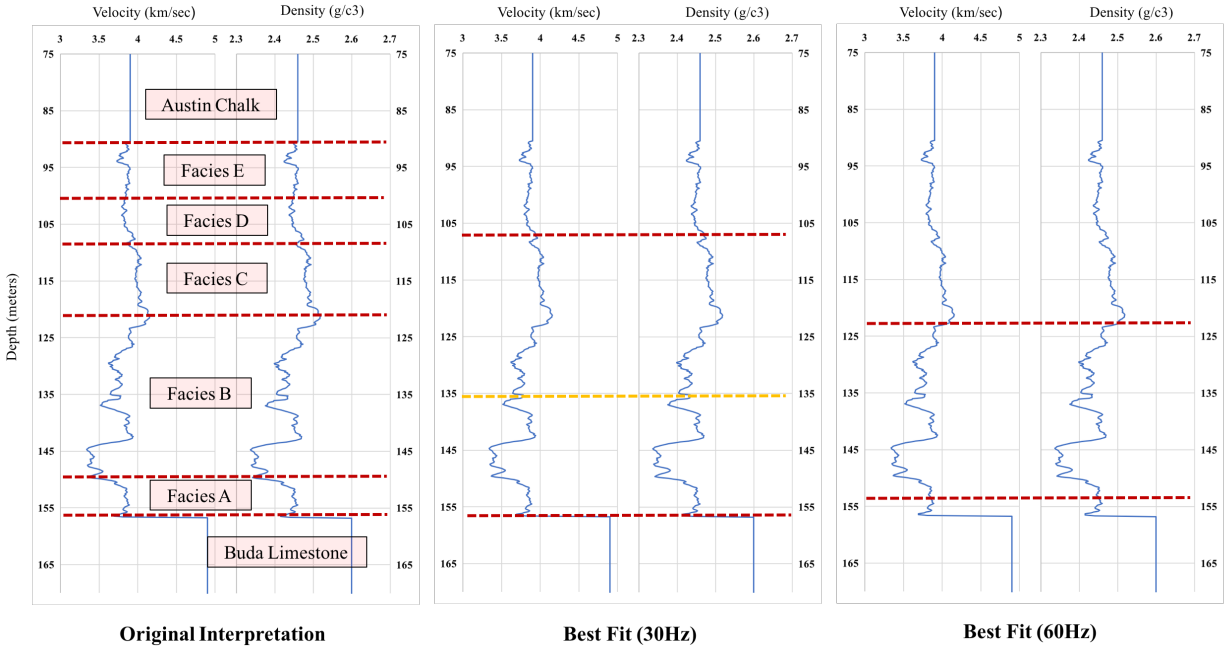

Figure B.3: Comparison of facies interpretation at Colonel Bend between original log interpretation (left), 30Hz best-fit upscaled model (center), and 60Hz best-fit upscaled model (right).

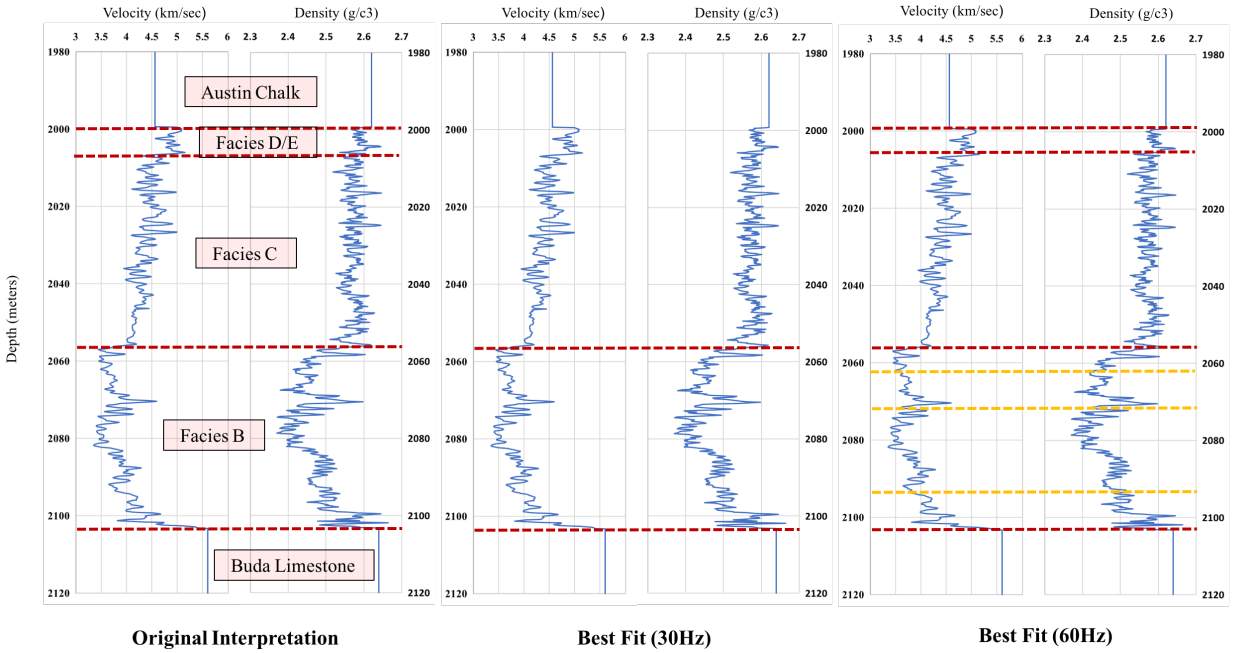

Figure B.4: Comparison of facies interpretation at Well 1 between original log interpretation (left), 30Hz best-fit upscaled model (center), and 60Hz best-fit upscaled model (right).

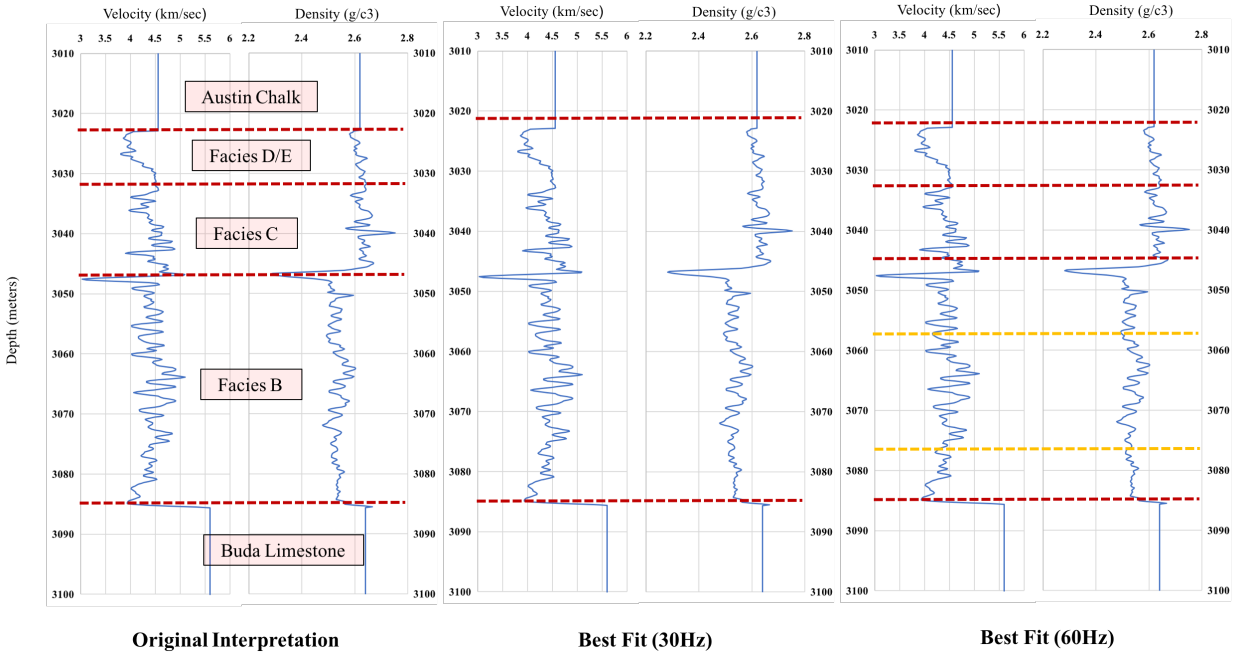

Figure B.5: Comparison of facies interpretation at Well 2 between original log interpretation (left), 30Hz best-fit upscaled model (center), and 60Hz best-fit upscaled model (right).

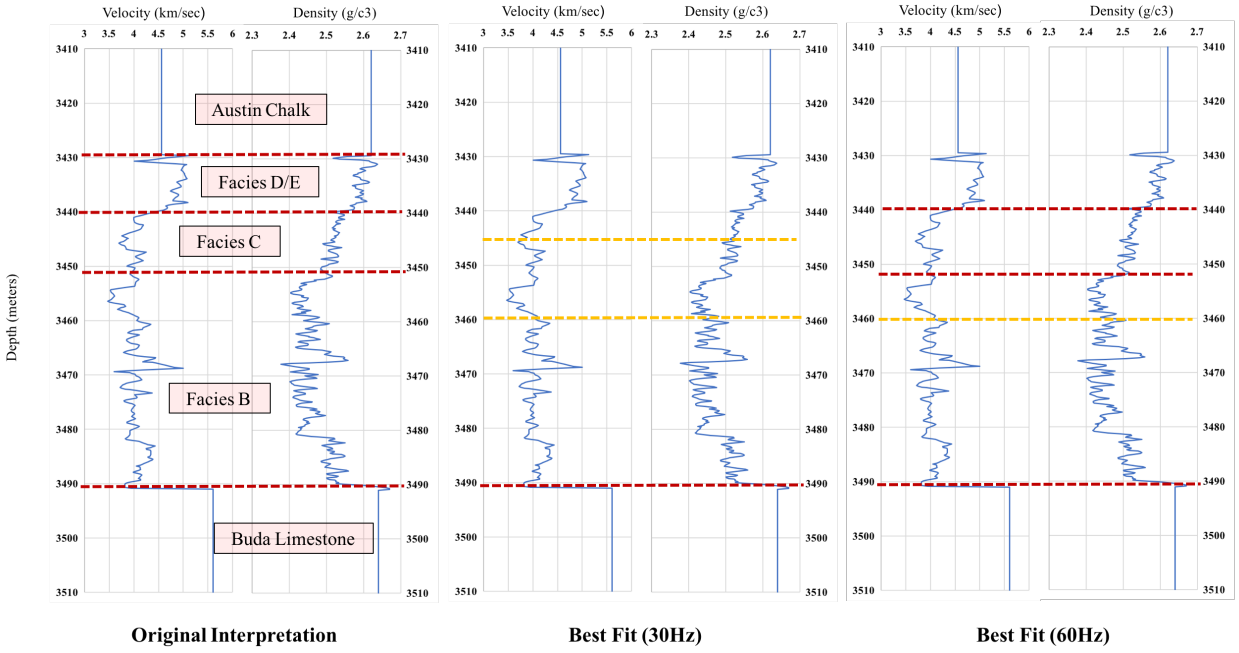

Figure B.6: Comparison of facies interpretation at Well 3 between original log interpretation (left), 30Hz best-fit upscaled model (center), and 60Hz best-fit upscaled model (right).

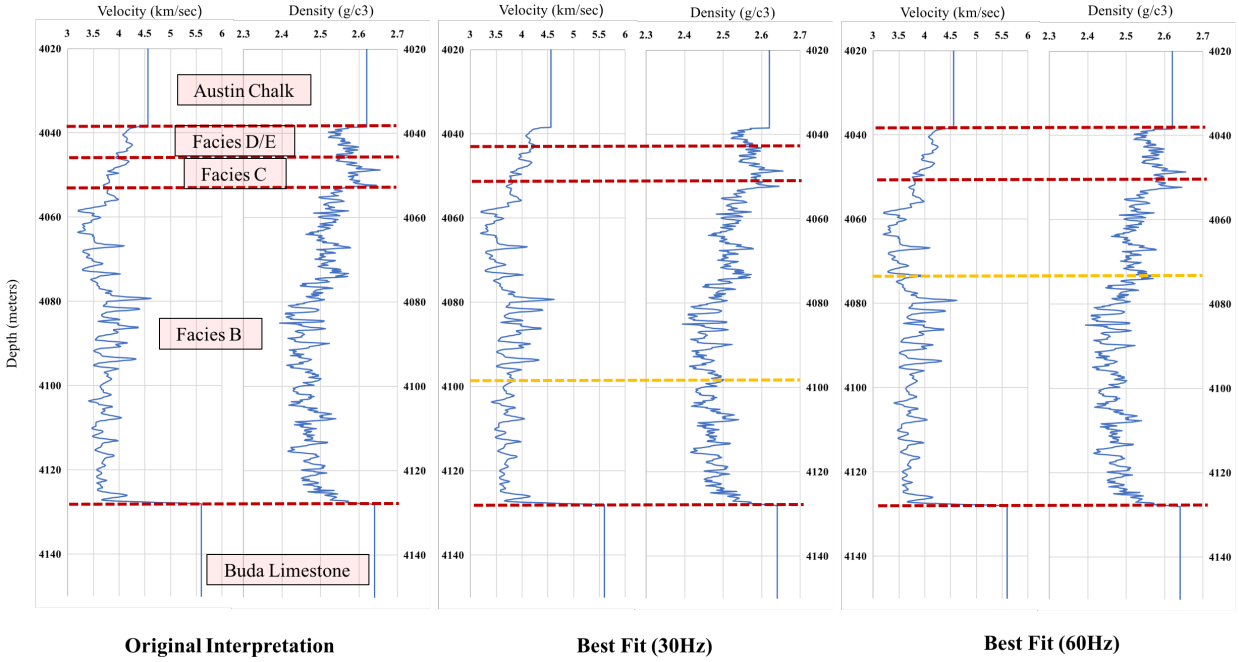

Figure B.7: Comparison of facies interpretation at Well 4 between original log interpretation (left), 30Hz best-fit upscaled model (center), and 60Hz best-fit upscaled model (right).